GRAPHENE OXIDE REINFORCEMENT IN PLASMA SPRAYED NICKEL-5% ALUMINUM COATINGS

by

DAVID B. WARD
B.S. Mechanical Engineering, University of Oklahoma, 2012

A thesis submitted in partial fulfillment of the requirements
for the degree of Master of Science in Materials Science and Engineering
in the Department of Materials Science and Engineering
in the College of Engineering and Computer Science
at the University of Central Florida
Orlando, Florida, USA

Fall Term
2014

Major Professor: Sudipta Seal

ABSTRACT

Metallic plasma sprayed coatings are widely used in the aerospace industry for repair on worn engine components. However, the inherent defects in these coatings limit the variety of repairs and reduce the service life of the repaired parts. A potential solution to overcome this problem is to mix small amounts of inexpensive graphene oxide in the powder feedstock. The incredible strength to weight ratio of graphene oxide makes it a viable additive to improve mechanical properties of metallic plasma sprayed coatings. The powder system chosen for this research is Nickel-5Aluminum since it is a common coating for such repairs. The greatest challenge was retaining graphene oxide, which combusts at 400°C, while melting the Nickel above 1450°C using a high temperature plasma plume. Graphene oxide was successfully retained in the coatings using either of two configurations: (1) Injecting the graphene oxide powder via solution suspension separately from the metal powder, or (2) Installing a shroud on the front of the plasma gun and backfilling with Argon to inhibit combustion. The uniquely designed solution suspension configuration resulted in a higher deposition efficiency of graphene oxide while the inert shroud configuration had a more homogeneous distribution and retention of graphene oxide in the coatings. The best overall coating was achieved using the inert shroud configuration using a powder mixture containing 2% weight Edge Functionalized Graphene Oxide. Vickers microhardness increased 46% and tensile adhesion strength increased 26% over control samples. This is possible due to the mechanisms of dislocation strengthening and stress transfer previously reported in graphene oxide reinforced Aluminum composites formed by flake powder metallurgy. It was also observed that the energy released by the combustion of graphene oxide helps to uniformly melt the

Nickel particles and improve the coating microstructure, allowing for more forgiving spray parameters. The methods developed and results attained in this research open opportunities for graphene oxide to be added as inexpensive reinforcements to other metallic compositions for widespread use in metal matrix composite manufacturing.

ACKNOWLEDGMENTS

I am sincerely grateful to Dr. Sudipta Seal for providing the opportunity to complete this thesis research under his direction. Special recognition goes to Ankur Gupta and Shashank Saraf for their assistance and guidance that greatly contributed to the success of this project. I must also thank Swetha Barkam for her help with SEM/EDS and Tamil Selvan Sakthivel for his help with tensile testing. Thank you to the personnel at Garmor, Inc for providing the Graphene Oxide, motivating us, and giving continual feedback. I must also acknowledge the U.S. Air Force S&E PAQ program for funding my tuition and labor during this Master's program.

TABLE OF CONTENTS

LIST OF FIGURES

LIST OF TABLES

CHAPTER 1: INTRODUCTION

Objective of Thesis

The objective of this research is to modify the properties of a commonly used metallic plasma sprayed coating by adding Graphene Oxide. There is no published information on Graphene Oxide being used in any thermal sprayed coating. Recent developments in cost-effective methods to mass produce Graphene Oxide powder allow it to be a viable reinforcement in existing bulk powder systems. The 95% Nickel-5% Aluminum powder system was chosen as the model system since it is simple and is commonly used in the aerospace industry. Positive results from this research could lead to the use of Graphene Oxide in many metallic plasma sprayed systems in industry.

Plasma Spray Method

Plasma spray is a type of thermal spray process used to deposit metallic, ceramic, cermet, and polymeric coatings. A feedstock (in this case, powder) is inserted to a plasma plume heat source and propelled toward a substrate. These molten or semi-molten particles deform in to lamellar layers upon impact and quickly solidify to create a coating. Several layers are applied using multiple passes by a pre-programmed robotic arm until the desired thickness is achieved [1]. Figure 1, below, illustrates the plasma spray process using the Praxair SG-100 gun.

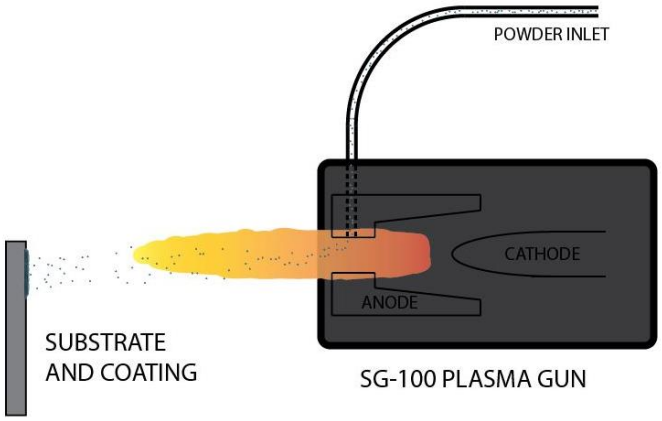

Figure 1: Typical Plasma Gun Setup with Internal Powder Injection

There are numerous parameters that must be carefully controlled to deposit quality coatings. Moreover, the substrate must be rough and clean for better adhesion. The end objective is for the particles to be at an appropriate temperature and velocity to allow proper wetting as they spread and solidify. A perfect combination of temperature, velocity, and substrate surface properties will create splats resembling flat discs [2]. Each powder and gun combination has a set of ideal parameters which relate to substrate conditions, heat source, or powder delivery. Some of these parameters are listed in Table 1.

Table 1: Plasma Spray Process Parameters

Substrate Conditions	**Heat Source**	**Powder Delivery**
Substrate Stand-off Distance	Plasma Arc Electric Power	Powder Mass Flow Rate
Substrate Angle	Plasma Arc Primary Gas	Powder Carrier Gas
Substrate Temperature	Plasma Arc Secondary Gas	
Substrate Surface Roughness		

Applications for Metallic Plasma Spray Coatings

Plasma spray coatings are commonly used in the automotive, aerospace, and shipbuilding industries for the manufacturing of new components and composites. A

substrate is used for bulk strength and the coating is used for surface modification (e.g. resistance to corrosion, abrasion, and/or heat). A well-known example of this are Thermal Barrier Coatings on gas turbine blades that allow operation at higher temperatures. In the case of metallic coatings, the component can be a less expensive material while the coating contains the surface properties desired for the specific application.

Metallic plasma spray coatings are also used for unique repairs on parts that were originally cast or rolled and did not have a coating. For example, many depot level repairs on gas turbine components require restoring worn metal back to original dimension. The build-up is done by thermal spraying, electroplating, or welding, followed by machining to obtain the required dimension. Each process has its benefits and drawbacks:

- **Electroplating** can coat geometries that thermal spraying and welding cannot, but the coatings are often brittle and the waste created by electroplating is hazardous to the environment and expensive to dispose of.
- **Welding** creates the strongest and thickest possible build-up, but requires heating the base metal to high temperatures, often altering the mechanical properties and microstructure. Additionally, many repairs take several hours and require concentration and a skilled hand.
- **Plasma spraying** is an effective and versatile method to evenly coat a large area with a machinable coating. However, plasma spray coatings contain numerous defects which cause them to be much weaker than a welded or casted component of equivalent composition. Additionally, residual stresses develop as the coating thickness increases, limiting the maximum thickness.

It is clear that these processes have many limitations. Some repairs cannot be done by any process, requiring replacement with a new, expensive part. There is great incentive in limiting the inherent weaknesses of plasma spray coatings to allow for more parts to be repaired. Special attention is paid to substrate preparation, process parameters, and powder composition in order to maximize the properties of these plasma spray coatings. This paper investigates if inserting an additive to a commonly used metallic powder could improve the properties of existing coatings.

Mechanical Properties of Ni-5Al Coatings

Ni-5Al plasma sprayed coatings are commonly used as build-up on metallic parts as well as bond coats for ceramic coatings. This composition makes for good all-around coatings with a maximum service temperature of 800°C. Its popularity and versatility has led to several studies to investigate, optimize, and model its properties.

Physical Structure

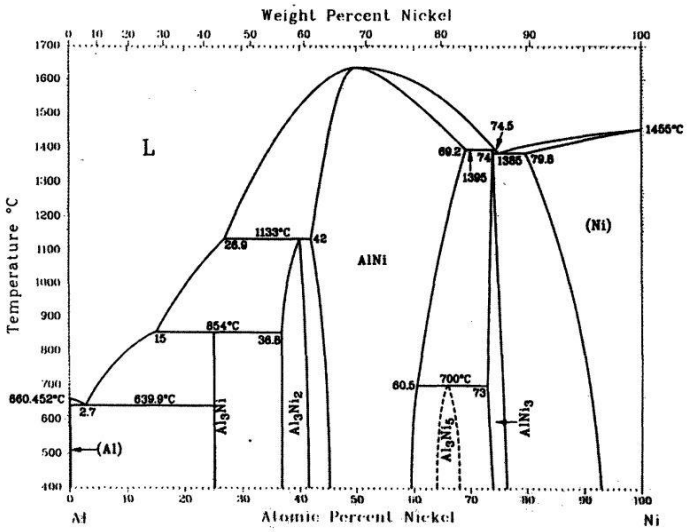

Figure 2: Nickel - Aluminum Phase Diagram [3]

The Nickel - Aluminum phase diagram above [3] indicates that a composition of 95% weight Ni and 5% weight Al exist as a solid solution and Ni_3Al intermetallic. It has been found that the Ni-5Al powder, when fed through the intense heat of a plasma plume, readily forms an intermetallic Ni_3Al phase. This Ni_3Al intermetallic phase enhances the coating's wear, oxidation, and corrosion resistance [4]. The remaining traces of the Aluminum atoms are dissolved into the face-centered cubic Nickel matrix or, if exposed to Oxygen, form Aluminum Oxide. The oxidation mechanisms in Ni-5Al thermal sprayed coatings were examined by Dr. Sampath's group at Stony Brook University [5]. The oxidation mechanisms laid out in their research aided in the microstructure analysis of the coatings created by the four configurations used in this thesis.

Microhardness

Mohamed S. Morsi et al. [6] conducted several experiments to create the ideal Ni-5Al bond coat for a Zirconia-based thermal barrier coating. Their optimum coating was 250μm thick with a Vickers microhardness of 190 H_V, a tensile bond strength of 35 MPa (5100 PSI), and a porosity of 2%. Their experiments demonstrate that these properties can diminish drastically by slight deviation from the optimum parameters. Another study reported microhardness values ranging 121 to 162 HV for plasma sprayed Ni-5Al coatings. This study also concluded that plasma spraying method makes a denser and more corrosion resistant Ni-5Al coating than the flame spraying method [7].

Tensile Bond Strength

Sulzer Metco, a leading manufacturer of thermal spray powders, advertises that 480NS (equivalent to Praxair Ni-185, used in this study) is rated for tensile adhesion strength up to 10,000 PSI, depending on equipment, process, and parameters [8]. Optimizing parameters for maximum tensile strength may be at the sacrifice of porosity, oxide content, wear resistance, corrosion resistance, and hardness. A balance must be achieved for the best overall coating.

It has been well-documented that the adhesion strength of metallic coatings degrades with increasing thickness due to residual stresses developed during splat solidification. Experts recommend to perform the ASTM C633 tensile test on coatings with a thickness of 250 microns [9]. A study conducted in 1992 on Ni-5Al concluded that a maximum tensile bond strength near 10,000 PSI can be achieved at 250 microns thickness, but a bond strength under 5,000 PSI is to be expected for coatings near 1mm thickness [10]. Two years later a model was fit to the available Ni-5Al data to approximate the tensile strength and residual stresses in the coating according to thickness [11].

Pre-heating the substrate can reduce coating porosity and increase the tensile bond strength [12]. This process removes moisture, promotes diffusion, and allows molten splats to flow freely in to crevices in the substrate which increases mechanical interlocking. A study was completed on the bond strength of pure Nickel coatings based upon the substrate temperature. Coatings sprayed on 25°C substrates resulted in an average bond strength of 10 MPa (1450 PSI) while coatings sprayed on 650°C substrates resulted in an average bond strength of 74 MPa (10,738 PSI) [12]. Substrate temperature likely has a similar effect on Ni-5Al coatings. It should be noted that pre-heating or post-

treatment annealing in many real-world applications is undesirable since it can warp parts and requires extra time and energy. It is for these reasons that we did not perform any pre-heating or annealing.

Graphene Oxide

The materials science community has shown substantial interest in graphene since it was isolated in 2004. Graphene is a 2D material consisting of sp^2 bonds between carbon atoms arranged in a hexagonal fashion. It has incredible mechanical strength (~1 TPa), thermal conductivity (5000 W m^{-1} K^{-1}), and charge carrier mobility at room temperature (250,000 cm^2 V^{-1} s^{-1}) [13]. However, it is very difficult to produce large quantities of graphene with few defects. Current manufacturing methods make it much easier to produce bulk quantities of lower quality Graphene Oxide. The properties of Graphene Oxide are not as good as those of pristine graphene, but it is a more cost-effective option for mixing in large quantities with thermal spray powder.

Graphene oxide can be synthesized using several methods. Most commonly, graphite is oxidized to graphite oxide using the Brodie, Hummers, or Staudenmaier method [14]. This oxidation increases the distance between the individual graphene layers in the graphite and allows for sonication or mechanical exfoliation to break the graphite oxide down to graphene oxide [13]. The resulting graphene oxide is hydrophilic due to its oxygenated functional groups on its basal planes and edges. A thin paper-like sheets have been obtained from graphene oxide and have demonstrated high mechanical strength up to 32GPa [15].

Graphene platelets can be produced by a chemical, electrochemical, or thermal reduction process from graphene oxide. The properties of this Reduced Graphene Oxide (RGO) can vary based upon the reduction process. RGO is hydrophobic and is one step closer in structure and properties to pristine graphene.

Graphene or graphene oxide composites prepared via different routes shown considerable improvement in the mechanical properties. For instance bulk aluminum reinforced with 0.3% weight graphene oxide (high quality, <5 layers) have been fabricated using flake powder metallurgy. The 62% increase in yield strength were attributed to dislocation strengthening and stress transfer [16]. The most extensive work using Graphene and Graphene Oxide for mechanical reinforcement are in ceramics prepared via spark plasma sintering. An improvement of 40% in fracture toughness was achieved for a Graphene-ZrO_2-Al_2O_3 composite formed by ball milling followed by spark plasma sintering. The graphene nanoplatelets inhibit fracture by a crack bridging mechanism [17]. Even better results were found in Silicon Nitride, where the graphene platelets congregated in the ceramic grain boundaries, resulting in a 235% improvement in fracture toughness [18]. However at this time no publications are known that use Graphene or Graphene Oxide in a thermal spray coating.

Carbon Nanotubes

A carbon nanotube is effectively a cylindrical shaped graphene sheet. It is for this reason that carbon nanotubes and graphene share similarly high mechanical properties. Single walled structures generally have diameters of 0.8-2nm while multi-walled carbon nanotubes typically have diameters of 5-20nm. Lengths are usually in the nano scale but can be achieved up to several centimeters [19].

The incredibly high specific strength of carbon nanotubes (~55.5 GPa/(mg/m^3)) make them ideal reinforcements to increase the mechanical properties of certain materials [20]. The past fifteen years has seen numerous publications involving carbon nanotubes reinforced composites formed by conventional sintering, spark plasma sintering, and hot extrusion. Several studies have proven that CNT added in Aluminum by these methods increases hardness, yield strength, ultimate tensile strength, and Young's modulus on a nano-scale [21] [22]. However, there are limitations in forming bulk CNT reinforced composites due to uneven distribution and a poor CNT to matrix interface. Recently, plasma spraying was used to form large CNT reinforced dogbone-shaped Al-Si coatings. These dogbone specimens were tensile tested, resulting in a 78% increase in elastic modulus, but a negligible increase in ultimate tensile strength [23]. Much better results were achieved in plasma sprayed CNT reinforced Aluminum Oxide coatings to increase tribological properties. Macro-wear resistance increased 49 fold with Al_2O_3 - 8%wt CNT over that of Al_2O_3 [24].

Hypothesis

Based on these observations, it is likely that graphene oxide reinforcement is possible in a Nickel-based metal matrix. The plasma spray deposition process will be used to achieve homogenous distribution of graphene oxide. This reinforcement may enhance the tensile strength, hardness, Young's modulus, and abrasion resistance.

CHAPTER 2: METHODOLOGY

Introduction

The greatest challenge in graphene oxide reinforcement is uniformly melting the nickel particles (at 1455°C) without burning away the Graphene Oxide (400°C). Innovative powder delivery and plasma spray methods were employed until an increased carbon content was confirmed within the coatings. Several powder mixing methods were attempted for uniform mixing and for homogeneous distribution of additive within the metal matrix. Coatings were extensively analyzed and tested for mechanical properties and corrosion resistance. Experiments and tests followed industry standards when possible and aimed to be thorough, consistent, and repeatable.

As-Received Powders

Nickel – 5 Aluminum

The Nickel – 5% weight Aluminum powder was procured from Praxair Ni-185. Its spheroidal particles are 45-90 micron diameter and are formed by water atomization. The following image displays the general size and shape of the Ni-185 particles. A common equivalent to Ni-185 is Metco 480NS. The aerospace industry uses hundreds (if not thousands) of pounds of these powders each year for bond coatings and dimensional buildup.

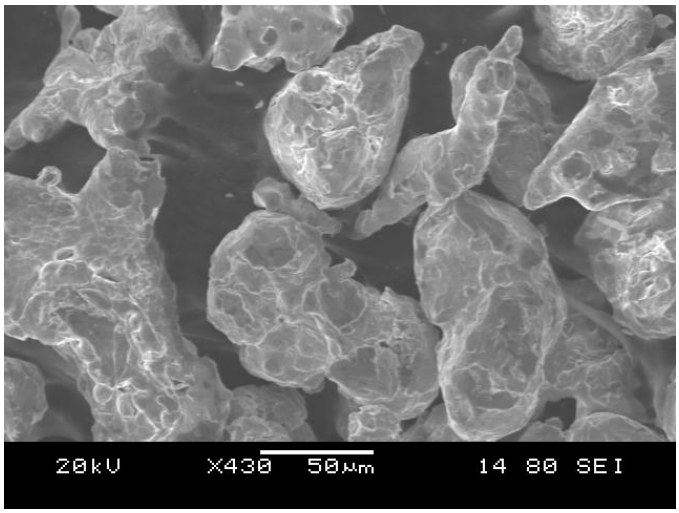

Figure 3: Scanning Electron Microscope Image of As-Delivered Ni-185 Powder

Ni-185 has been approved by the Original Equipment Manufacturer (OEM) to be used in the following repair specifications:

Canada Pratt & Whitney CPW 490
CFM International CP 6007 (except moisture)
General Electric B50TF56, Cl B
GKN Aerospace PM 819-56 (special order)
Honeywell EMS 57746, Type I, Cl 1
Pratt & Whitney PWA 1380
Rolls-Royce plc MSRR 9507/5

Graphene Oxide

The Graphene Oxide powder used is manufactured by Garmor, Inc. in bulk quantities with large-scale industrial application in mind. The particles have an average of 10 graphene sheets. The Edge Functionalized Graphene Oxide (EFGO) contains approximately 91 atomic % Carbon and 9 atomic % Oxygen. The Reduced Graphene Oxide (RGO) contains approximately 98.5 atomic % Carbon and 1.5 atomic % Oxygen. The figure below contains the de-convoluted X-Ray Photoelectron Spectroscopy (XPS) analysis on the as-received graphene oxide particles.

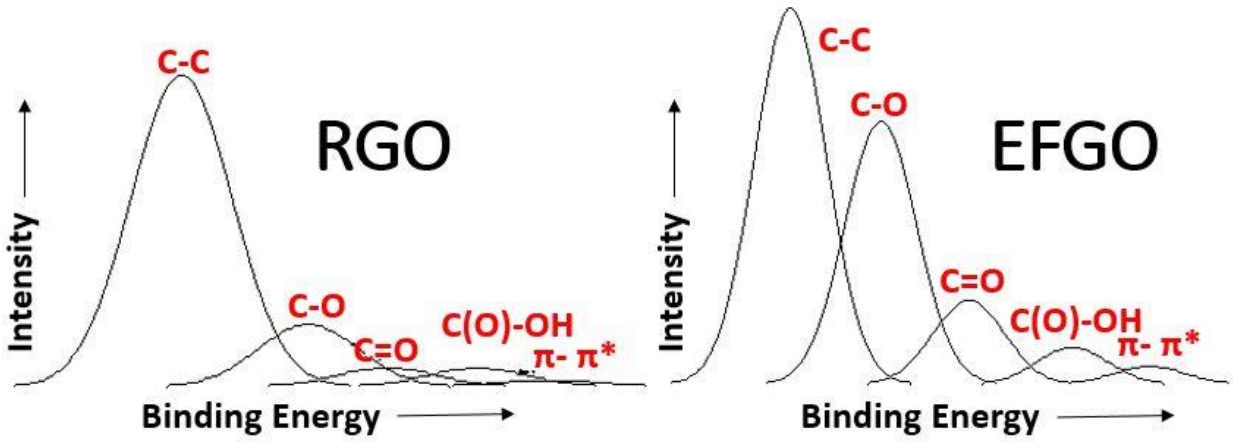

Figure 4: XPS Analysis on Carbon Bonds in RGO (Left) and EFGO (Right)

Multi-walled Carbon Nanotubes

The Multi-walled Carbon Nanotubes (MWCNT) were procured from Sigma Aldrich. These are non-functionalized and produced by catalytic chemical vapor deposition. The MWCNT have an outer diameter 10-15 nm, inner diameter 2-6 nm, length 0.1-10 μm, and have Carbon content >90%.

Powder Mixing, Milling, and Suspension

Very little published information exists related to the mixing behavior of Graphene Oxide or Carbon Nanotubes with Nickel-based powders. This section details the mixing methods used and analysis on the characteristics of each mixture.

Jar Mixing of Graphene Oxide with Ni-185

Several mixing techniques were attempted to achieve a uniform mixture of Graphene Oxide and Ni-185. Compositions ranged from 0.5% to 4.0% weight Graphene Oxide with remaining Ni-185 powder. The Graphene Oxide particles are nano-sized with

many micron-sized agglomerations and are black in color. The Ni-185 particles are 45-90 micron sized and silver in color.

Jar mixing on horizontal rollers for 5 minutes produces a solid black mixture that looks uniform upon visual inspection. The smaller Graphene Oxide particles readily stick to the outer surface of the much larger Ni-185 particles. However, many larger Graphene Oxide agglomerations did not break up or stick to the Ni-185. The jar mixing was continued for up to 24 hours and at speeds between 80 and 150 RPM and using both glass and plastic containers, but the large Graphene Oxide clusters remained agglomerated.

Figure 5: Stock Ni-185 (Left) and Jar Mixed Ni-185 & 1% wt EFGO (Right)

Best results for jar mixing Graphene Oxide and Ni-185 were achieved by adding 3.55g stainless steel pellets. A ball-to-powder weight ratio of 1:5 was used. The low ball-to-powder ratio, low 100 RPM speed, and soft plastic container were all used in an effort to only break up the Graphene Oxide agglomerations without deforming the malleable Ni-185 powder or causing damage to the Graphene Oxide. Total mass between 50 grams and 200 grams were successfully mixed using this method. The figure below shows an SEM image of a 99% wt Ni-185 and 1% wt EFGO mixture after 6 hours of low energy jar milling. It can be seen that the Ni-185 particles were not deformed.

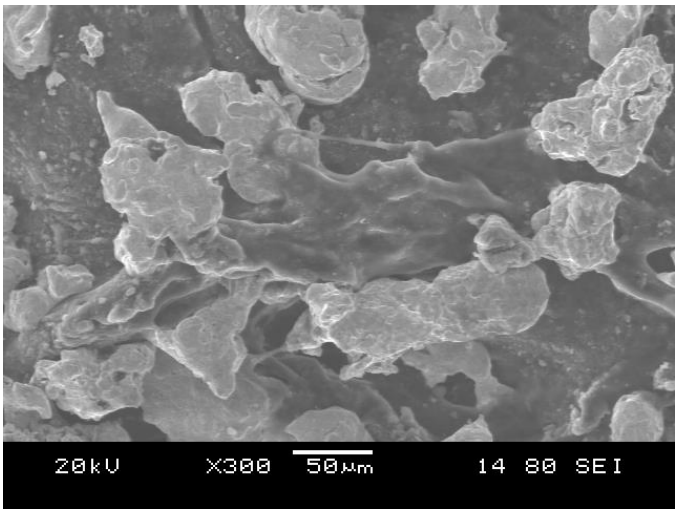

Figure 6: SEM Image of Ni-185 and 1% wt EFGO after Jar Mixing

ResoDyn Acoustic Mixing of Graphene Oxide with Ni-185

A ResoDyn LabRAM acoustic mixer was successfully used to mix Ni-185 with EFGO. A mass of 99 grams of Ni-185 and 1 gram of EFGO were mixed with an intensity of 50 G's for 10 minutes. This mixing method certainly creates a uniform mixture of Graphene Oxide and Ni-185, though SEM imaging could not distinguish between this mixture and that created by jar milling with pellets.

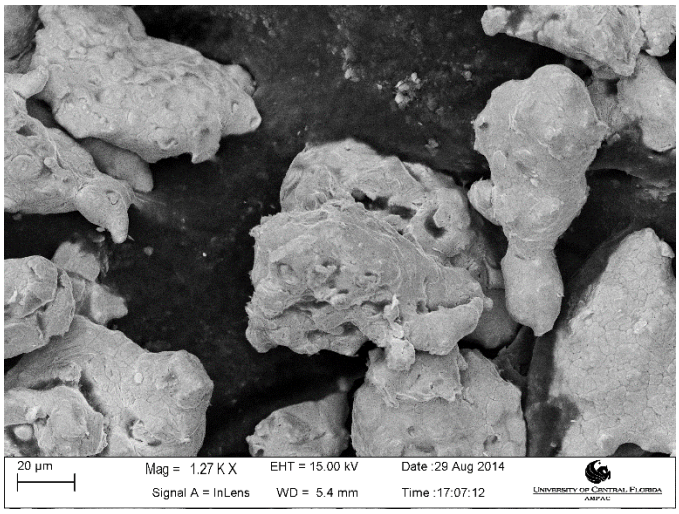

Figure 7: SEM Image of Ni-185 and 1% wt EFGO after Acoustic Mixing

Jar Mixing of Carbon Nanotubes with Ni-185

Simple jar mixing of CNT and Ni-185 does not create a mixture. There is little cohesion between the CNT particles and the Ni-185 particles, and the Ni-185 are much denser than the CNT, so the two powders immediately separate. A mixture of 98% weight Ni-185 and 2% weight CNT was jar mixed with 3.55g stainless steel pellets for 8 days to no avail. The image below is the CNT and Ni-185 powder after 8 days in the jar mixer. Gentle shaking of this tray further separated the CNT and Ni-185 to the point that the Ni-185 powder remaining was indistinguishable from untouched Ni-185 powder.

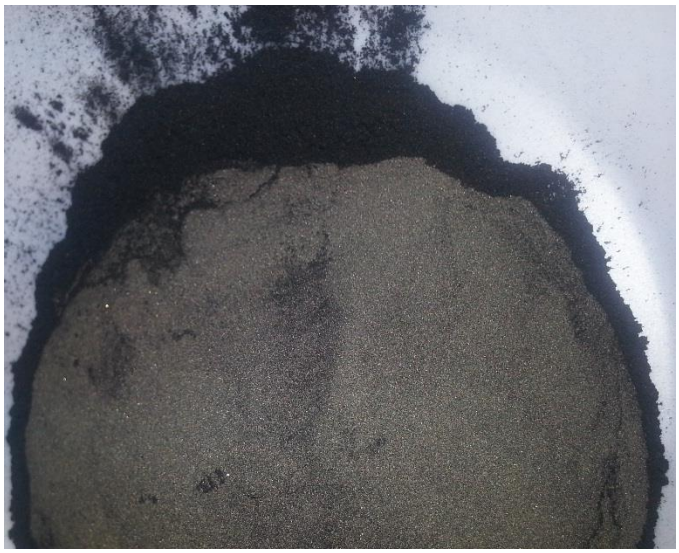

Figure 8: Photo of Ni-185 and 2% wt CNT after 8 Days Jar Mixing

ResoDyn Acoustic Mixing of Carbon Nanotubes with Ni-185

The CNT and Ni-185 were put in the ResoDyn LabRAM acoustic mixer. Settings of 50G, 30G, and 80G were used for 10 minutes each, but still the powders would not mix. The majority of the CNT caked on the bottom of the plastic LabRAM container and had to be scratched off to be retrieved. The image below is the mixture after 30 total minutes in the acoustic mixer. Gentle shaking of this vial further separated the CNT and Ni-185 after this photo was taken.

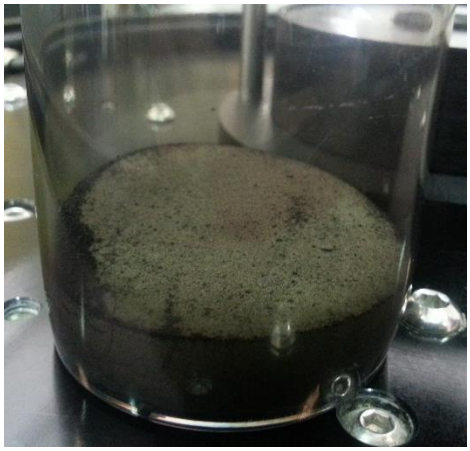

Figure 9: Photo of the Ni-185 and 1% wt CNT after Acoustic Mixing

Using a Binder to Mix Carbon Nanotubes with Ni-185

Using a polymer binder was held as a last-resort since the presence of the binder in the plasma sprayed coating could negate any positive effects created by the CNT reinforcement. High energy ball milling was considered but was not used since ball milling severely damages or even cuts the CNT. It is likely that even the low energy jar milling used in this project causes a measurable amount of morphological change to the CNT [25].

Two different polymer binders resulted in successful uniform mixtures of CNT and Ni-185. The first used was liquid 3-aminopropyl-trimethoxysilane (APTMS). A mass of 190 grams Ni-185 powder was mixed with 8 mL APTMS in the jar mixer for 2 hours. Then the 198 gram mixture was placed in a glass container in an oven at 100°C for 2 hours. The majority of the APTMS vaporized and the remaining mass was 190.2 grams. The powder was very clumpy and stuck to the walls of the container. A mass of 189.9 grams was able to be removed. 5 grams of CNT were added for a final composition of 2.56% wt CNT. The

mixture was placed in a plastic container on the jar mixer at 100 RPM with 20 3.55g stainless steel balls (2.75:1 powder to ball ratio) for 24 hours.

The second binder used was 1400 molecular weight (powder) Polyethylene Glycol (PEG). Only 1 gram of PEG was required to successfully mix the 200 total grams (196g Ni-185 and 4g CNT) that would not mix after 8 days in the jar mixer. 6 additional hours of jar mixing with PEG resulted in a mixture that would not separate, as seen in the following image.

Figure 10: Image of Ni-185 and 2% wt CNT Mixture with PEG Binder

Ball Milling of Ni-185

Simple mixing of the Ni-185 with graphene oxide results in the Nickel particles being coated with graphene oxide flakes. This does not provide much protection for the graphene oxide in the harsh plasma plume. A. Esawi et al. [26] successfully dispersed CNT *within* Aluminum powder particles by a combination of ball milling and low energy jar

mixing. The Al particles were first flattened and broken apart in the ball mill, then the particle size grew due to cold welding. A similar process was attempted with the Ni-185 particles but was unsuccessful. The Ni-185 particles immediately cold welded to each other and to the metallic walls of the planetary ball mill. The process was attempted again with a small amount of Toluene in the powder, but this time they would not cold-weld back together. The Nickel particles more readily cold welded to the metallic walls of the ball mill than to each other, so the process was stopped. The experiment might be successful if attempted inside of a Teflon coated container. The SEM image below is of the Ni-185 particles after total 24 hours (5 minute on/off intervals) in the planetary ball mill. A 10:1 ball to powder ratio was used. Enough Toluene was added every 4 hours to keep the particles damp.

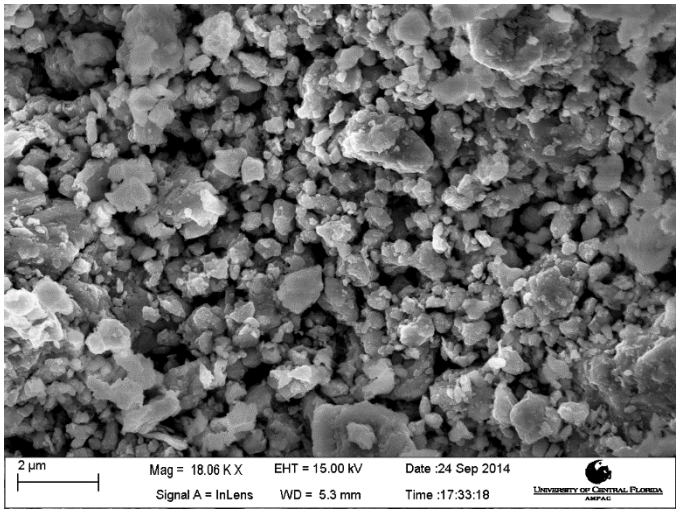

Figure 11: SEM Image of Ball Milled Ni-185 Powder

Scanning electron microscopy indicates the original 45-90 µm particles were reduced in size to 0.5-10 µm. A simple test was conducted to see if these small particles would suspend in water. A small amount (~0.1 gram) of this fine powder was added in 5

mL of deionized water and sonicated for 1 minute. The particles successfully dispersed in the water but settled after several hours. No dispersion whatsoever is possible with the large 45-90 μm Nickel powder. Spray drying from a solution of ball milled Ni-185 powder, EFGO, and deionized water may be possible. It was not attempted in this experiment since it would require a large amount of processing time and tuning of parameters to yield enough powder to be usable for a plasma sprayed coating.

Thermodynamic Analysis of Powders

Differential Scanning Calorimetry (DSC) was performed on all powders (EFGO, RGO, CNT, and Ni-185) separately in the air and an inert environment. All tests had a temperature ramp rate of 10°C/minute to a final temperature of 900°C. The initial weight loss seen in the region up to ~120°C is due to water evaporation. Any weight loss after that point is due to combustion. The heat flow curve trending downwards indicates that the machine is required to add heat to the system in order to increase the temperature. The exothermic peaks in the heat flow curve indicate the powders are releasing energy in to the system via combustion. The following figures contain the DSC results and the table at the end of this section summarizes for all findings.

Differential Scanning Calorimetry on EFGO

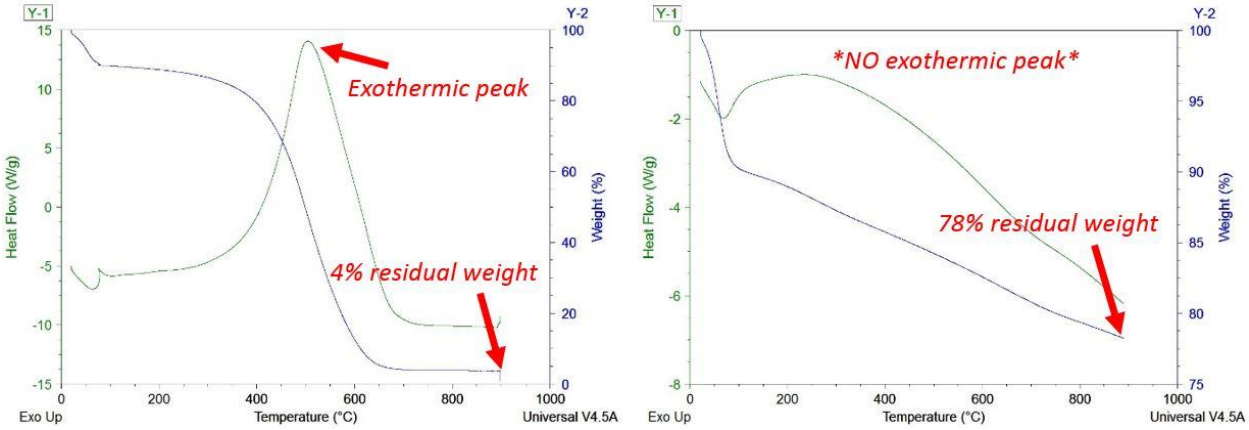

Figure 12: DSC Analysis on EFGO Powder in Air (Left) and Argon (Right)

The curves in the figure above indicate that EFGO begins combustion near 375°C in the presence of Oxygen. Approximately 96% of its weight burns away. In the absence of Oxygen the EFGO does not combust and was able to retain 78% of its weight. Weight loss rate in the Argon environment stays constant as temperature increases. Approximately 1% of total weight is lost during the final 10 minutes of the process from 800°C to 900°C.

Differential Scanning Calorimetry on RGO

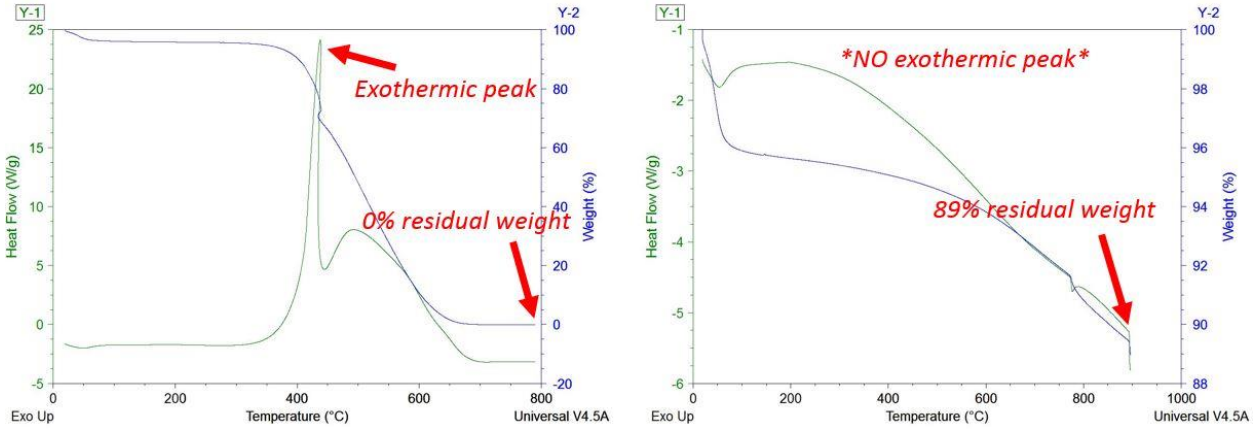

Figure 13: DSC Analysis on RGO Powder in Air (Left) and Argon (Right)

The curves in the figure above indicate that RGO begins combustion near 375°C (the same as EFGO) in the presence of Oxygen. However, 100% of its weight is lost. In the absence of Oxygen the RGO does not combust and is able to retain 89% of its weight. The weight loss rate in the inert environment slowly increases as temperature increases. The mass loss rate is lower than that of EFGO at lower temperatures but is the same for the final 10 minutes of the process from 800°C to 900°C.

Differential Scanning Calorimetry on MWCNT

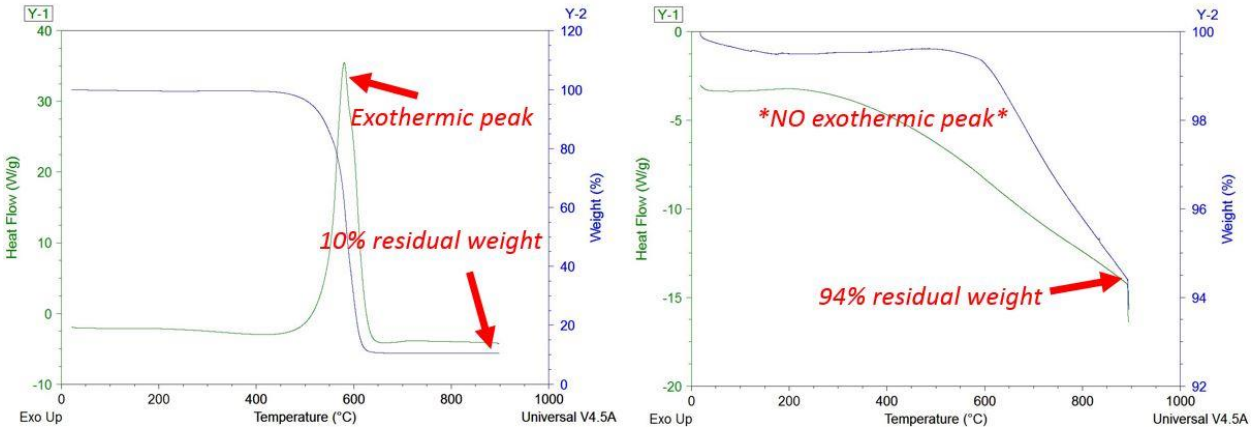

Figure 14: DSC Analysis on MWCNT Powder in Air (Left) and Argon (Right)

The curves in the figure above indicate the MWCNT begins combustion near 500°C in the presence of Oxygen and 90% of its weight is lost. The remaining 10% was orange in color and is due to the Catalytic Chemical Vapor Deposition used to produce these MWCNT. In the absence of Oxygen the MWCNT does not combust and is able to retain 94% of its weight. It hardly loses any weight up to 600°C then has a constant weight loss rate all the way to 900°C.

Differential Scanning Calorimetry on Ni-185

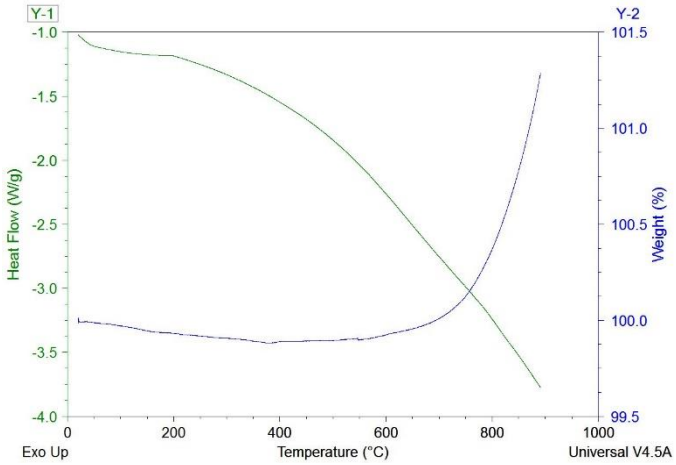

Figure 15: DSC Analysis on Ni-185 Powder in Air Environment

The weight increase in the figure above is a result of oxidation. The heat flow for the entire temperature range is negative, meaning that there are no phase changes in the metal at this range.

DSC Summary and Discussion

The following table summarizes the results from several DSC tests. The MWCNT are the most likely to survive a brief moment in the intense heat of a plasma plume since they have the highest combustion temperature and a multi-walled structure. All three powders have similar exothermic enthalpy with RGO being the highest and EFGO being the lowest. This is likely because RGO has the lowest oxygen (highest carbon) composition and EFGO has the highest oxygen (lowest carbon) composition.

Table 2: Summary of Differential Scanning Calorimetry Data

Powder	Atmosphere	Combustion Temp.	Residual Weight at 900°C	Exothermic Enthalpy
EFGO	Air	375-650°C	4%	11,740 J/g
EFGO	Argon	N/A	78%	N/A
RGO	Air	375-650°C	<1%	13,682 J/g
RGO	Argon	N/A	89%	N/A
MWCNT	Air	500-625°C	10%	13,281 J/g
MWCNT	Argon	N/A	94%	N/A
Ni-185	Air	N/A	101.25%	N/A

The direction of this research was determined early based upon this Differential Scanning Calorimetry data. Combustion of the additives occur in the presence of Oxygen at or below approximately 650°C. This is troublesome since the temperature of the plasma plume is 10,000+°C and the Ni-185 particles must achieve a temperature above 1,455°C to melt. The good news is the DSC curves indicate that the combustion is not rapid. It took several minutes at the slow temperature ramp rate 10°C/minute for each additive to finish combustion. Therefore, it is clear that the mixed powders must only be exposed to an inert environment to prevent burning off the additive.

The maximum service temperature of sprayed Ni-5Al coatings is advertised by the powder manufacturers as 800°C. A small amount of oxidation in the Ni-185 powder was observed beginning at 700°C. It is uncertain if the volatility of the graphene oxide or the CNT above 400°C in the presence of Oxygen could reduce the maximum service temperature of these coatings. No high temperature testing was done on the coatings themselves. However, it has recently been proven that graphene nanoplatelets inside of

a TaC matrix formed by spark plasma sintering can survive the heat of a plasma torch. [27]

Substrate Preparation

Identical preparation was used for all substrates. Substrates used are 1/8” thick 316L stainless steel. This substrate was chosen since it is a commonly used steel and has a similar thermal expansion coefficient (~16.5 x 10^{-6} m/m/K) to Nickel (~13 x 10^{-6} m/m/K). Substrates were not pre-heated. The following table contains the seven steps followed for every substrate prior to plasma spraying.

Table 3: Substrate Preparation Process

Step 1	Cut to approximately 20 mm x 40 mm with hack saw
Step 2	Grind and sand edges to remove burrs
Step 3	Clean with acetone
Step 4	Grit blast using -100+400 mesh Alumina grit at 4” standoff distance at 70 PSI for approximately 30 seconds
Step 5	Clean with acetone immediately after grit blast
Step 6	Place substrate on fixture
Step 7	Clean with acetone immediately before plasma spraying

Plasma Spray Methods and Arrangements

Several arrangements were attempted in order to melt the Ni-185 (1450°C) without burning the graphene oxide (400°C). Two basic approaches were taken. The first was to surround the particles in an inert atmosphere during spraying so there could be no combustion or oxidation. The second was to pass the Ni-185 powder through the hottest part of the plasma plume and simultaneously pass the additive through a cooler part of the plasma plume.

SG-100 Gun, Standard Configuration

This configuration simply uses the Praxair SG-100 gun with internal powder injection to insert the particles in to the hottest part of the plasma plume. The simplicity and versatility of this configuration have led to its common use in industry. This SG-100 plasma spray gun has multiple anode and cathode options allowing for energy levels up to 80 kW and gas velocity ranging from subsonic to Mach II. The primary gas used is Argon, so theoretically the powder traveling in the center of a low-turbulence plume would not be exposed to Oxygen. Some turbulence always occurs but was minimized by avoiding the use of cooling air jets. Below is an illustration of this configuration and a table with the spray parameters that were most commonly used. A detailed list of parameters have been provided in the Appendix.

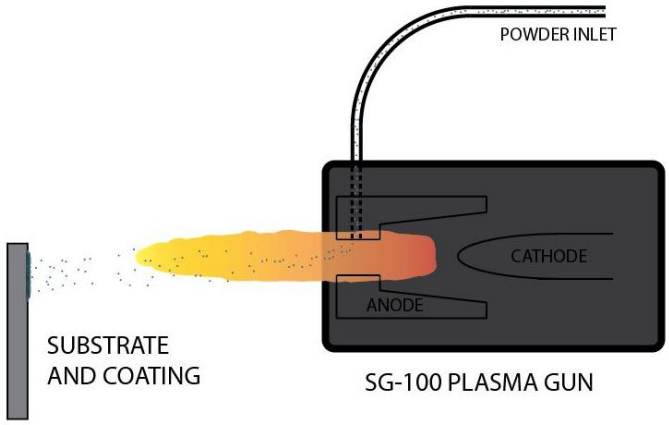

Figure 16: SG-100 Gun with Internal Powder Injection

Table 4: SG-100 Spray Parameters

Current	Primary Gas	Secondary Gas	Power	Standoff Distance
600 Amps	85 SCFH Argon	10 SCFH Hydrogen	18 kW	115 mm

SG-100 Gun with Inert Shroud Configuration

This is a modification on the usual SG-100 configuration. A shroud is added to the front of the gun and is backfilled with Argon at 15 PSI during the spraying process. The objective of this configuration is to create an inert environment in the local area that the particles are at high temperature. This inhibits combustion of the graphene oxide and reduce the formation of aluminum oxide.

The configuration has its limitations. First, the plasma plume can only run for about 60 seconds before the shroud and cooling system risk overheating. Second, the shroud used is quite heavy, so the robot must travel at slower speeds to keep from triggering its alarm sensors. Third, the added parts on the front of the gun create a minimum standoff distance of 100 mm.

The same gun parameters as the regular SG-100 configuration were used. A diagram of the Argon shroud configuration is below. Notice the particles are in an inert environment while inside the shroud. Possible turbulence could briefly expose the particles to Oxygen in the small gap between the substrate and the shroud.

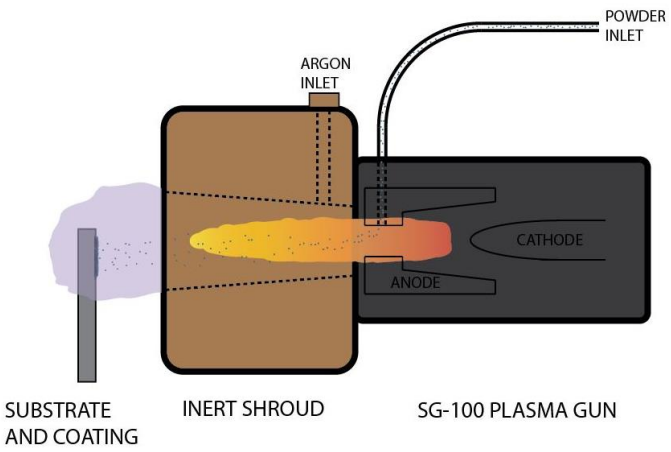

Figure 17: SG-100 Gun with Inert Shroud Configuration

F4 Gun, Standard Configuration

This configuration simply uses the Sulzer F4 gun. This gun is widely used due to its reliability and simplicity. It differs from the previous two configurations in that it uses an external powder injection method. Argon carrier gas pushes the powder through an external nozzle at such a velocity that it is able to penetrate in to the center of the plasma plume. Too much or too little carrier velocity will result in inadequate particle heating. Its powder nozzle is larger than the SG-100's nozzle, so a high deposition rate is more easily achieved.

The primary drawback of this configuration in the context of this experiment is that it exposes many of the high temperature particles to Oxygen. As seen in the figure below, the powder is inserted in the top of the plume and the molten particles spread as they are propelled toward the substrate. The molten particles outside of the plume are at higher risk of in-flight oxidation (or combustion in the case of graphene oxide).

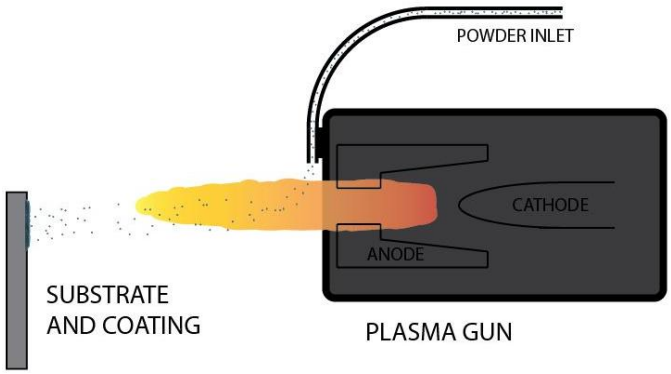

Figure 18: F4 Gun with External Powder Injection

Table 5: F4 Spray Parameters

Current	Primary Gas	Secondary Gas	Power	Standoff Distance
600 Amps	85 SCFH Argon	20 SCFH Hydrogen	22 kW	150 mm

F4 Gun with Solution Suspension Configuration

This is a modification to the normal F4 configuration. The Ni-185 powder is carried in to the hot part of the plume as usual while a liquid solution is inserted separately in to a much cooler part of the plume. A deionized water solution was used to suspend 0.5% weight EFGO. An ethanol solution was used to suspend 0.1% weight RGO. The solution injection point was set so the solution would reach a temperature such that the water or ethanol would quickly vaporize (100°C and 78°C, respectively) while the graphene oxide would not combust (400°C). The solutions were sonicated immediately prior to spraying and a compressed air atomizer was used as the solution injection nozzle.

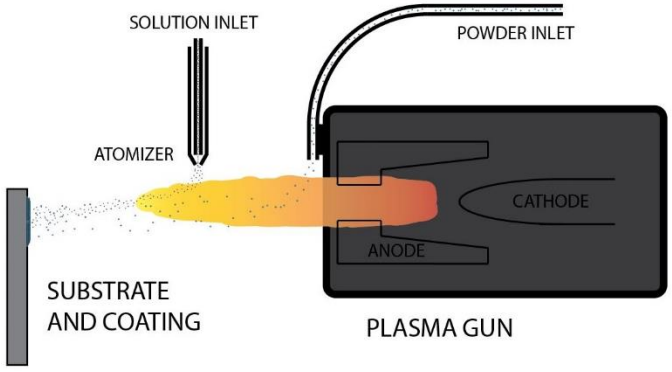

Figure 19: F4 Gun with Solution Suspension Configuration

Coating Characterization and Testing

Coating Processing

Coating thickness was measured with a micrometer between spray cycles until a desired thickness was reached. Many coatings were rinsed with water and sprayed with compressed air to observe any color change. Samples were then cut, mounted in epoxy resin, and polished to study the cross-section. The following polishing process was used for all cross-sections. The polish was deemed worthy if it was easy to find a field of view under a 40x optical microscope with no visible scratches.

Table 6: Cross-Section Polishing Process

Step 1	SiC 120 grit with water
Step 2	SiC 400 grit with water
Step 3	SiC 800 grit with water
Step 4	SiC 1200 grit with DiaPro 9μm diamond suspension lubricant
Step 5	MD-Dac with DiaPro 3μm diamond suspension lubricant
Step 6	Polishing cloth with alumina powder
Step 7	Clean with acetone
Step 8	Inspect with 40x optical microscope for scratches

Optical Microscopy

The 40x optical microscope lens on a Shimadzu HMV-2T microhardness tester was used for microstructure analysis of the cross-section. It was used for measuring average coating thickness, observing splat boundary morphology, and inspecting the interface between the coating and substrate. Images were taken of each coating and ImageJ software was used to quantify the “irregularities” (pores + oxides) in the microstructure. The result is a percent of irregularities, as seen in the following figure, which was used to qualitatively compare the microstructures. All images were taken in succession on the same day to ensure each image to avoid the variation in brightness,

contrast, magnification, and scale. All images were identically scaled, cropped, converted to 8 bit, and converted to binary so the particle identification function in ImageJ could consistently quantify these irregularities.

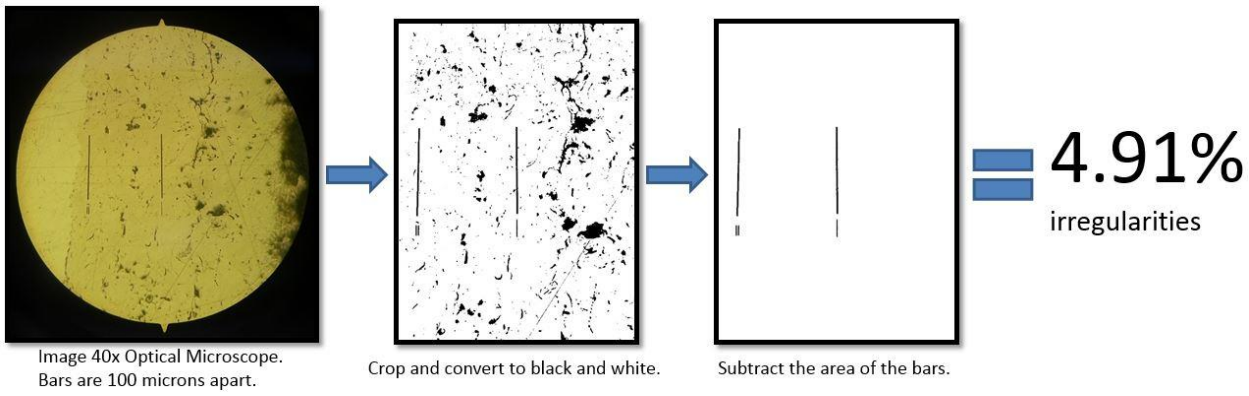

Figure 20: ImageJ Process to Quantify Irregularities

Microhardness Testing

The Vickers microhardness tester used is a Shimadzu model HMV-2T. Several forces and durations were tested to see which had the lowest standard deviation of hardness values. The test scale HV 0.5 (4.903 N) for 20 seconds was chosen. The cross section of each coating was polished and leveled, often multiple times, until indentions were symmetric and consistent. Usually indentions are invalid if the diamond-shape is in any way asymmetric or strangely shaped. However, some irregularity is expected and tolerated due to the presence of pores and oxides in plasma sprayed coatings. The indention in the following photo shows the most asymmetry that was tolerated.

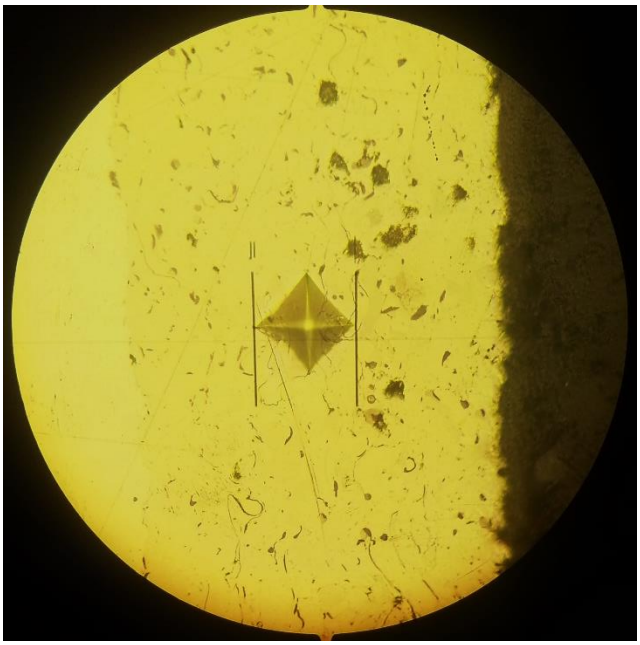

Figure 21: Typical Vickers Microhardness Indentation

The average of at least seven different tests were used to determine the microhardness of each coating. The following figure contains the distribution of the first seven tests throughout the cross section of each coating. Indentions 1, 2, & 3 were placed in the center of the coating. Indentions 4 & 6 were placed with their center approximately 150 microns from the substrate interface. Indentions 5 & 7 were placed with their center approximately 150 microns from the surface of the coating. The highest and lowest value were omitted. Tests beyond the first seven (starting over with location #1) were conducted until the standard error was 6 HV or less.

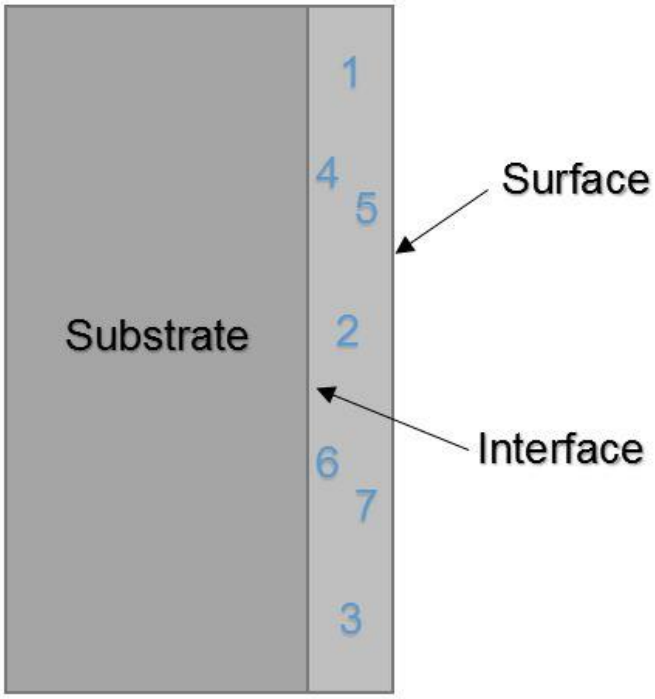

Figure 22: Microhardness Indent Locations

A side experiment was conducted to determine how the resulting microhardness value is affected by the microstructure targeted by the indention. On average, indentions aimed at irregularities (pores, scratches, and Aluminum oxide) resulted in a very high standard deviation and low hardness values. Indentions aimed away from irregularities resulted in a much lower standard deviation and ~15% higher hardness values on average. All microhardness values given in this study are from indentions that were aimed to avoid irregularities when possible. It is worth mentioning that (with 300+ indention sample size on 25+ different coatings) that the indentions closer to the substrate were, on average, 1% harder than those in the middle of the coating. Indentions closer to the substrate were, on average, 5% harder than those near the surface of the coating.

The diagonal widths of the indentions were usually around 70 microns. The dimensions of the indentions are used to calculate the microhardness of the material by the following (simplified) equation:

$$Vickers\ Hardness = \frac{Force}{Area} = \frac{1.8544 * F}{d^2}$$

where F is the force (in kgf) and d is the mean of the two diagonal widths (in mm). Using this equation the units of Vickers Hardness are in kgf/mm^2, though the units of Vickers Hardness are usually reported as HV. Tables exist for isotropic metals that estimate the tensile strength based upon the microhardness. These tables were not used because these coatings have many defects, are anisotropic, and the hardness values were only taken by indenting the cross section.

Tensile Testing

Bond strength testing was performed to ASTM C633 (Adhesion of Cohesion Strength of Thermal Spray Coatings) standards using additional recommendations from ASM Thermal Spray Society. [9] All tensile tests were performed by an Instron machine with Series IX software. The only deviation from their recommendations is the use of a self-aligning tensile machine, which was not available. The tensile strength values attained by this non self-aligning tensile tester may be slightly lower than those using a self-aligning tensile tester.

The ASTM C633 tensile configuration measures the adhesion of the coating to the substrate and the cohesion within the coating. The next figure displays the tensile test configuration using the coating sprayed on a 1” +0/-0.005” diameter button.

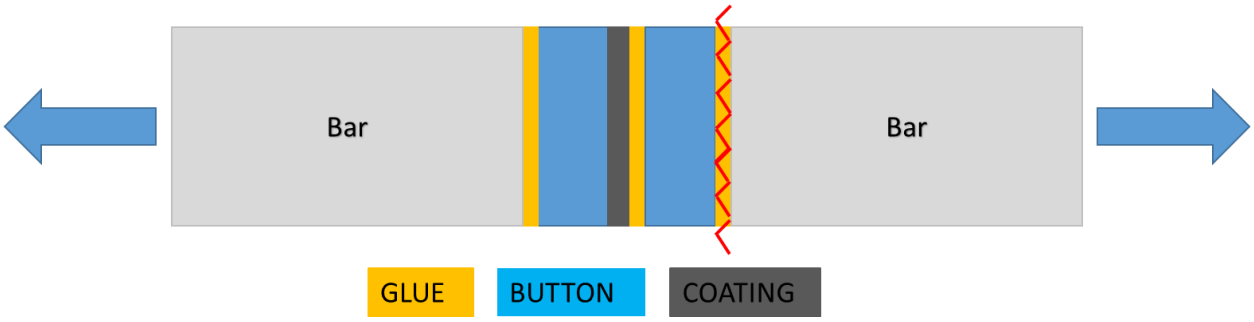

Figure 23: Tensile Test Configuration

Three distinct failure modes are observed: glue failure, mid-coating failure, and coating-interface failure. Most coatings failed by only one mode, some coatings failed by two modes, but the following photo is of one coating that failed by all three modes. In this case it is not clear which failure mode occurred first, triggering the other two failure modes.

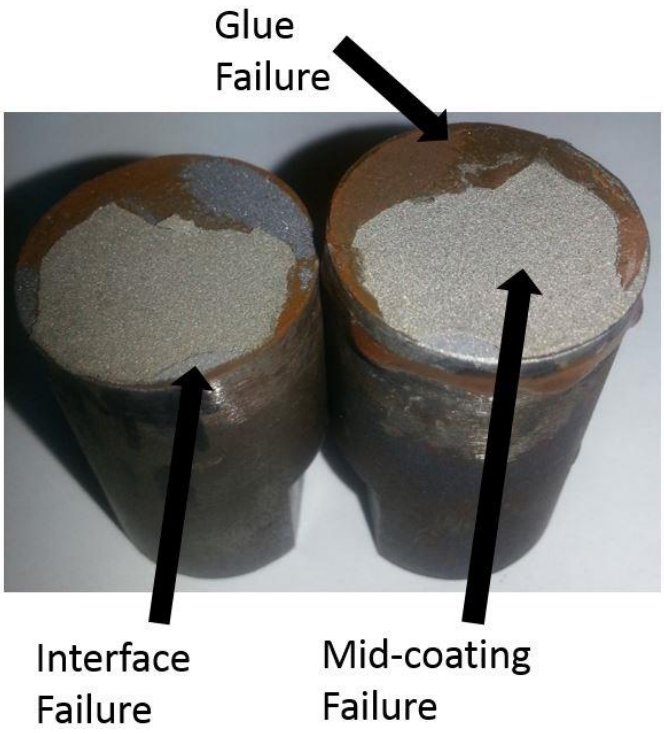

Figure 24: Tensile Break with all Three Modes of Failure

The tensile strength of each coating is given by the equation:

$$Tensile\ Strength = \frac{Force}{Area} = \frac{F}{\Pi * D^2/4}$$

where F is the force (in pounds) and D is the diameter of the cross-section area (in inches). The resulting units are PSI but are also commonly given in MPa for this test. Strain, Young's modulus, and elongation to failure are not considered since these would be skewed by the glue.

Scanning Electron Microscopy

A Zeiss Ultra 55 Scanning Electron Microscope (SEM) was frequently utilized on the cross-sections, fracture surfaces, and powders. Several SEM images of each coating were used in side-by-side comparisons to determine how the variation of one parameter or powder composition changed the splat boundary, interface, and oxide morphology.

Energy Dispersive X-Ray Spectroscopy

Energy Dispersive X-Ray Spectroscopy (EDS) was performed using a Noran System 7 with Silicon drift detector on a Zeiss Ultra 55 SEM. This method was used to determine the elemental composition (Ni, Al, O, and C) of each coating. It certainly has its limitations in quantifying smaller elements, such as Carbon, but identical inspections were performed on all cross-sections to at least provide a qualitative comparison. EDS was also very helpful in pinpointing Aluminum Oxide phases and determining the distribution of carbon in the coatings.

Tribology Testing

Tribology testing was performed by Dr. Arvind Agarwal's research group at Florida International University. Weight loss and coefficient of friction (COF) are measured during the ball on disk wear method. Tests were performed at room temperature in an ambient environment on the rough top surface of as-sprayed coatings. A 3mm alumina ball was used with a force of 10N. The track diameter was 8mm, speed was 200 RPM, and test duration 30 minutes.

CHAPTER 3: RESULTS

This thesis research had a very large scope. Four different plasma spray configurations and four different additives were used. The plasma spray process itself has over a dozen parameters. To keep the experiments focused, process parameters for each configuration were held constant once a good control sample was created. The remaining variables were additive concentration and powder mixing method. Even after imparting these limitations, 41 unique coatings were created to thoroughly analyze the behavior of each configuration and/or additive. Many of these 41 unique coatings were produced and inspected multiple times to ensure repeatability. The results are presented in a series of claims to organize the many trends observed.

Claim #1: Graphene Oxide Increases Microhardness

The most obvious and consistent trend observed is that the microhardness increases by the addition of graphene oxide. This was observed for all four configurations (SG-100, SG-100 with Argon shroud, F4, and F4 plus solution suspension), for all additive amounts (0.1 - 4.0 weight %), and for both mixing methods (jar mixing and acoustic mixing). The following table contains the microhardness data for all configurations, additive amounts, and mixing methods that were tested.

Table 7: Microhardness for all Configurations, Compositions, and Mixing Methods

Configuration	Additive (mix)	Microhardness	Std. Error	Change
SG-100	Control	171 HV	6 HV	
SG-100	1% EFGO (jar)	212 HV	5 HV	+24%
SG-100	1% RGO (jar)	186 HV	5 HV	+9%
SG-100 + Argon shroud	Control	161 HV	6 HV	
SG-100 + Argon shroud	0.5% EFGO (jar)	180 HV	5 HV	+12%
SG-100 + Argon shroud	1% EFGO (jar)	194 HV	4 HV	+20%
SG-100 + Argon shroud	1% EFGO (acoustic)	181 HV	2 HV	+12%
SG-100 + Argon shroud	1% RGO (jar)	177 HV	6 HV	+10%
SG-100 + Argon shroud	1.5% EFGO (jar)	230 HV	5 HV	+43%
SG-100 + Argon shroud	2% EFGO (jar)	249 HV	3 HV	+55%
SG-100 + Argon shroud	3% EFGO (jar)	232 HV	5 HV	+44%
SG-100 + Argon shroud	4% EFGO (jar)	216 HV	3 HV	+34%
F4	Control	161 HV	6 HV	
F4	1% EFGO (jar)	187 HV	5 HV	+16%
F4	2% EFGO (jar)	181 HV	6 HV	+12%
F4 + Solution Suspension	Control (H_2O)	155 HV	5 HV	
F4 + Solution Suspension	0.5% EFGO in H_2O	204 HV	6 HV	+32%
F4 + Solution Suspension	Control (Ethanol)	159 HV	2 HV	
F4 + Solution Suspension	0.1% RGO in Ethanol	205 HV	5 HV	+29%

The most complete set of microhardness data was collected for coatings containing jar mixed EFGO that were sprayed through the Argon shroud. Many of these coatings were sprayed, polished, and tested multiple times to ensure a small enough standard error to confidently publish these microhardness values. As seen in the following bar graph, a clear trend is observed with diminishing returns beyond 2% weight EFGO.

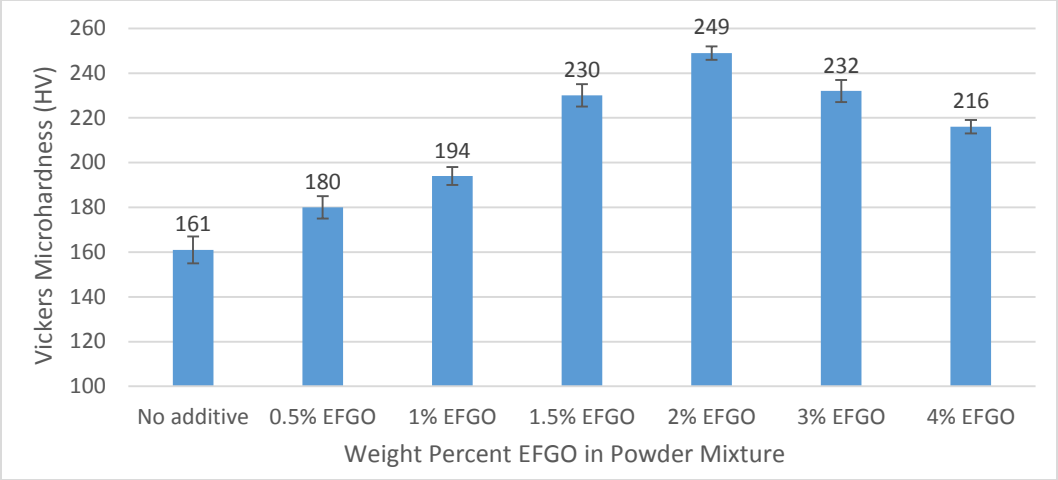

Figure 25: Vickers Hardness of Ni-Al-EFGO Coatings via Argon Shroud

Others have published microhardness values for Nickel-5Aluminum plasma sprayed coatings at 121 – 162 HV and 190 HV. [6] [7] As explained in detail in Chapter 2, the microhardness values can vary based upon polish quality and location of indentions, so it is a relief that the control samples in this study fall between those reported elsewhere. The highest microhardness value achieved by a control sample is 171 HV by the SG-100 normal configuration. Thus, the hardest coating with graphene oxide yields a 46% increase in microhardness over the hardest control.

Claim #2: Graphene Oxide Increases Tensile Strength

Select coatings were chosen for tensile testing. On average, coatings with graphene oxide failed at higher loads than the control samples. However, the standard deviation is quite high primarily due to glue failure. The bar graph below displays the results.

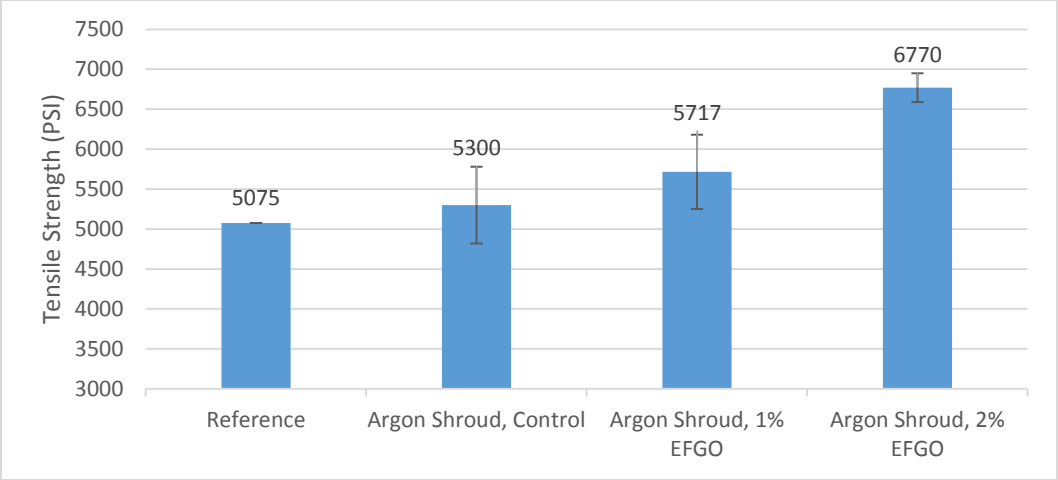

Figure 26: Tensile Strength Increase with Graphene Oxide

The error bars on the figure are standard error. Many more of each coating would need to be tested to truly distinguish between the reference [6], the control sample, and the coating with 1% EFGO. Also, the thickness of these coatings are similar but not identical. The tensile strength decreases with increasing thickness due to buildup of residual stress. [11] A thicker coating also has more potential area for failure. With that being said, the coatings with 2% EFGO are definitively stronger than the others.

Claim #3: Graphene Oxide Reduces Coefficient of Friction

It is clear from the ball on disk tests that the wear characteristics of the Argon shroud coatings are superior to those of the other configurations tested. This reinforces what was observed in their microstructures and microhardness values. The following figure contains the change in coefficient of friction (COF) over time for several coatings.

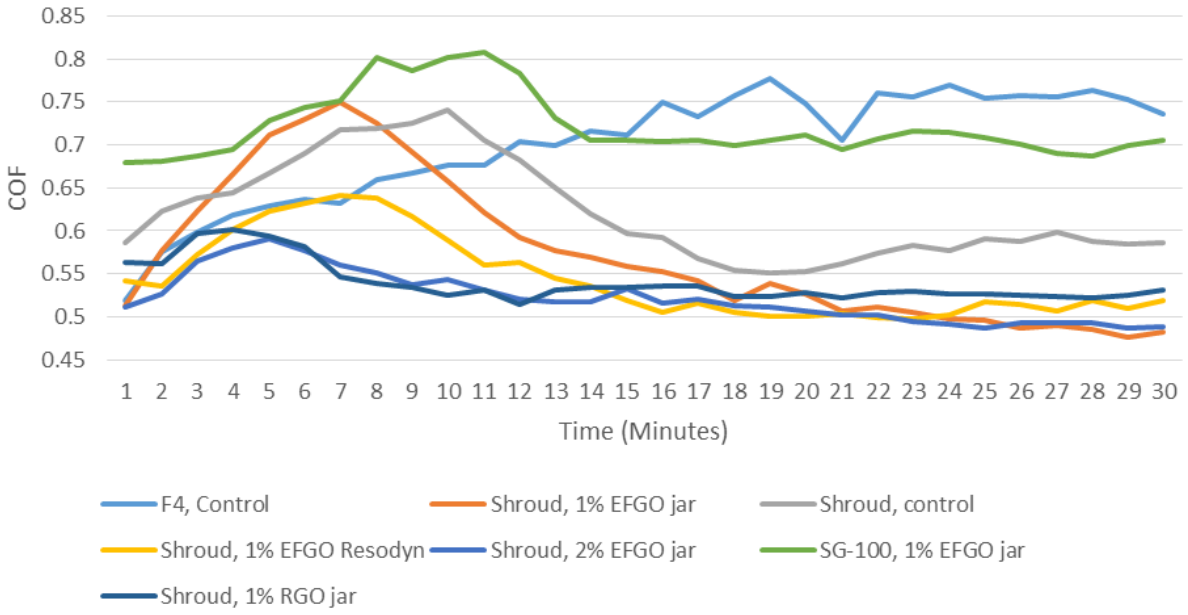

Figure 27: Change in Coefficient of Friction Over Time During Ball on Disk Wear Testing

The COF is stabilized after 30 minutes. The data reveals that the addition of EFGO or RGO results in a lower COF. The four lowest COF values are of coatings sprayed through the inert shroud. This confirms the general correlation between microhardness and wear properties. Weight loss measurements were also taken but were inconclusive since these tests were conducted on very rough as-sprayed surfaces. Ni-185 coatings are almost always ground or machined before real-world service, but were not for this test to eliminate possible bias.

Claim #4: Mechanical Enhancement Can be One of Many Mechanisms

As discussed in the Introduction chapter, graphene oxide reinforcement in other materials has been attributed to crack bridging, stress transfer, and dislocation strengthening [17] [18]. High magnification SEM imaging was performed on cross sections and fracture surfaces of the Ni-Al-GO plasma sprayed coatings. Remnants of

these strengthening mechanisms were not explicitly observed, but are likely present. The following SEM images are of two fracture surfaces at 11,000x magnification of coatings that were sprayed using the Argon shroud configuration. These are surfaces obtained by mid-coating failure from tensile testing.

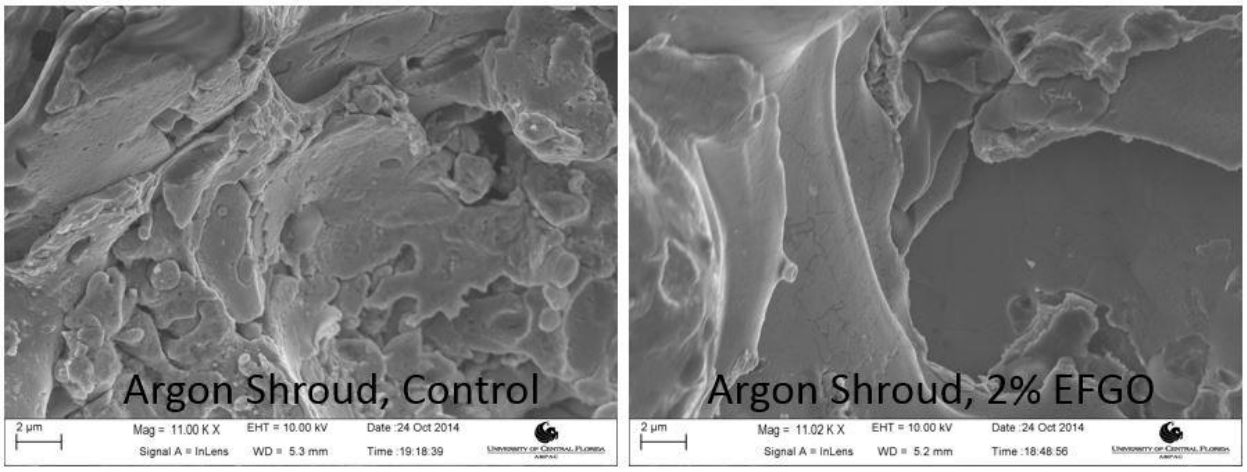

Figure 28: Fracture Surface of Control (Left) and Coating Containing EFGO (Right)

The fracture surface on the left is of the pure Ni-185 coating. The fracture surface on the right is of a coating created from a powder containing 2% weight EFGO. This coating containing EFGO had approximately a 55% higher microhardness and 25% higher tensile strength than the control. It is clear that the fracture surface of the coating with EFGO is much smoother than the fracture surface of the control. This smoothness allows for better cohesion between splats. The following images are of their cross section microstructure.

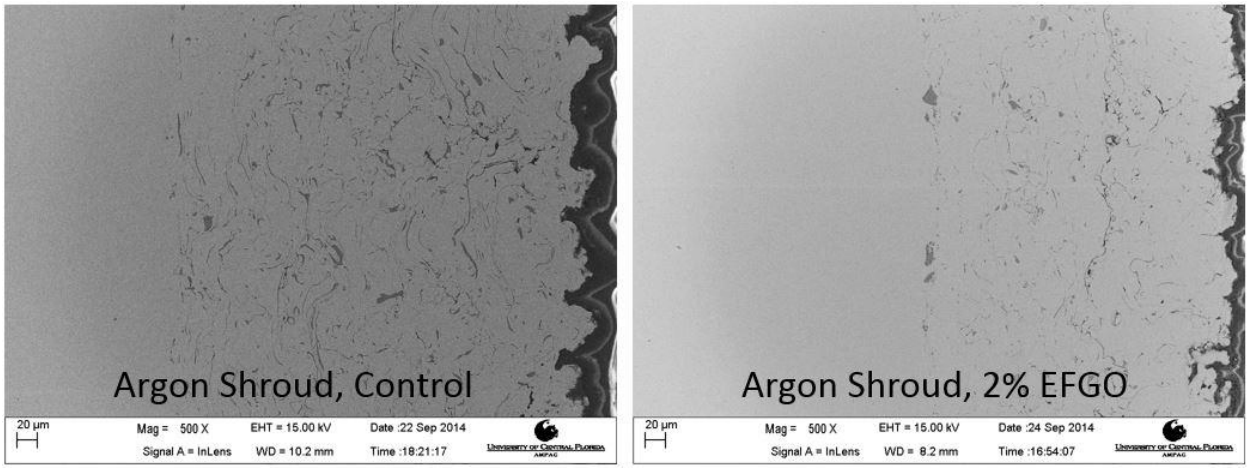

Figure 29: Microstructure of Control (Left) and Coating Containing EFGO (Right)

The microstructures are not drastically different, but there are certainly fewer dark irregularities within the coating containing EFGO (4.91%) than in the control (8.08%). These are Aluminum Oxide. The presence of these in the splat boundaries is one explanation for changes in the mechanical properties and a possible cause for the rough fracture surface.

Another possibility is the graphene oxide affecting the development of residual stresses. The stress might be relieved if the multi-layered graphene oxide structure is oriented in such a way that they layers can slide across each other during the rapid cooling process. Additionally, the heat transfer and thermal expansion coefficients of the bulk Nickel matrix are modified by graphene oxide presence, so that may play a role in the buildup of residual stresses.

There may be a thermodynamic mechanism that is enhancing the coatings. It is possible the exothermic energy from combusting graphene oxide assists in melting the Nickel particles. A sample was sprayed with pure Ni-185 powder using the F4 gun at very

low energy levels. The coating immediately peeled from the substrate after 5 spray cycles. The test was repeated using a powder mixture containing 1% EFGO. This coating did not peel from the substrate even after 20 cycles and had an adhesion strength of 2150 PSI. This is not a good adhesion strength, but is certainly better than zero. The bad interface and microstructure (below) make it clear that these low energy parameters are not ideal, but this result indicates that a powder mixture including graphene oxide could allow for more lenient process parameters.

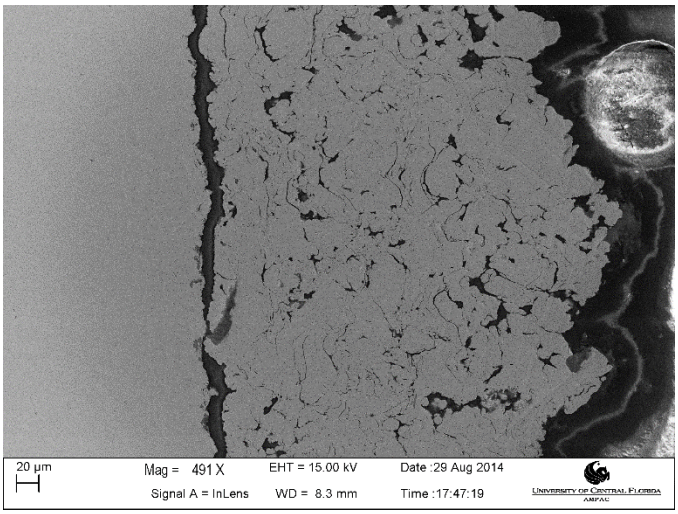

Figure 30: Microstructure of Low Energy Sprayed Coating with 1% EFGO

Claim #5: Graphene Oxide Reduces Deposition Rate

An obvious trend observed while creating coatings is the greater amount of Graphene Oxide present in the powder, the thinner the resulting coatings. Given a few assumptions, the deposition rate of the control sample sprayed through the Argon shroud was calculated for all coatings using the following equations:

$$Deposition\ Rate = \frac{Thickness}{Coating\ Exposure\ Time}$$

$$Deposition\ Rate = \frac{Thickness}{\frac{Spray\ Width}{Traverse\ Speed} * Passes\ per\ cycle * Total\ Cycles}$$

Calculated for the Argon shroud control sample:

$$Deposition\ Rate = \frac{400\mu m}{\frac{12mm}{50mm/s} * 4 * 3} = 139\ \pm 9\ \mu m/s$$

Average coating thicknesses were measured with an error of ±25 μm due to thickness irregularities. The spray width was crudely estimated to be 12 mm for the purposes of this calculation. The traverse speed is the lateral velocity of the robot as the gun passes the substrate. Based upon the robot's pre-programmed ladder path and the 12 mm spray height, it is estimated that a given point on the substrate is passed four times per program cycle. Three cycles were used for all coatings created with the Argon shroud configuration. The downward trend is illustrated in the following figure.

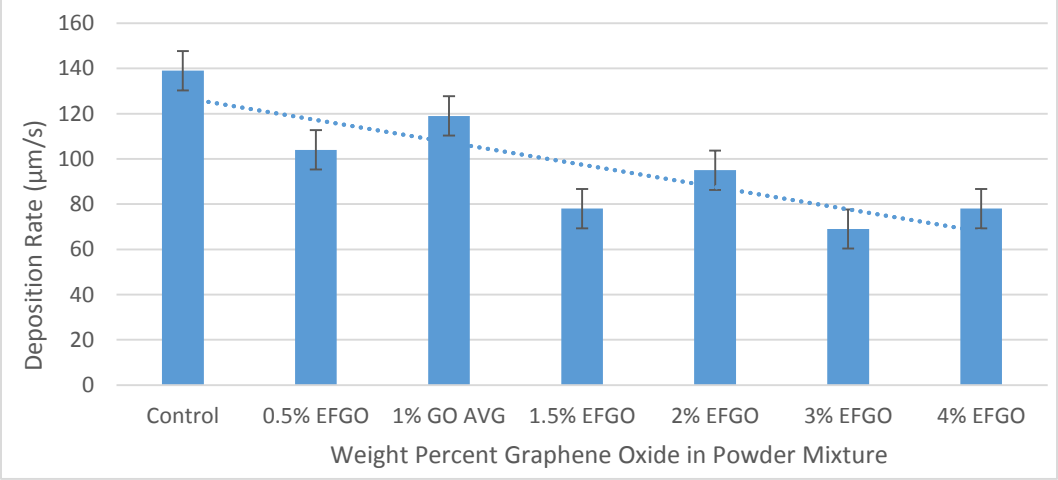

Figure 31: Deposition Rate Decrease with Increasing Graphene Oxide

This tendency relates to the way the powder feeder operates. Two parameters held constant for all experiments, no matter the configuration, are the speed of the powder

feeder (2 RPM) and Argon carrier gas flow rate (8.5 SCFH). The carrier gas is set for consistent powder flow and to propel the powder at the particular velocity required to penetrate the plasma plume. The powder feeder has a rotating disc with many small “pockets” that fill with powder before delivery to the plasma gun through a hose. The rotation speed corresponds to a certain volume flow rate. As Graphene Oxide is added to the Ni-185 the density decreases. Since the powder feeder effectively operates at constant volume flow rate, the increase in Graphene Oxide reduces the density of the powder mixture and reduces the mass flow rate. The consequential deposition rate is proportional to this mass flow rate.

Claim #6: Powder Composition has Limited Effect on Carbon and Oxygen Content within Coating

Carbon content detected within the coating is noticeably greater in coatings with Graphene Oxide than in the control samples. Oxygen content detected within the coating is noticeably less in coatings with Graphene Oxide than in the control samples. These trends were observed for all three configurations that were tested. The Carbon and Oxygen contents were the averages from multiple measurements at multiple locations and magnifications using. The following table contains the averages collected by EDS with an error near ± 0.4%.

Table 8: Carbon and Oxygen Content Retained in Coatings

Configuration	Additive	Weight Carbon	Weight Oxygen
SG-100	Control	0%	5.7%
SG-100	1% EFGO	1.8%	3.3%
SG-100	1% RGO	1.8%	2.1%
SG-100 + Argon Shroud	Control	0.6%	1.7%
SG-100 + Argon Shroud	1% EFGO	1.6%	1.0%
F4 + Solution Suspension	Control (H_2O)	0%	4.5%
F4 + Solution Suspension	0.5% EFGO in H_2O	5.2%	2.2%
F4 + Solution Suspension	Control (Ethanol)	0%	4.5%
F4 + Solution Suspension	0.1% RGO in Ethanol	9.8%	3.0%

After seeing this trend, more data was collected to see how much Carbon can be retained using powder mixtures with high Graphene Oxide quantities. The Argon shroud configuration was used. The next figure displays the negligible changes in Carbon and Oxygen content when any more than 1% EFGO is mixed in. The amount of EFGO in the powder mixture can be quadrupled, yet the Carbon and Oxygen in the coating remain within error.

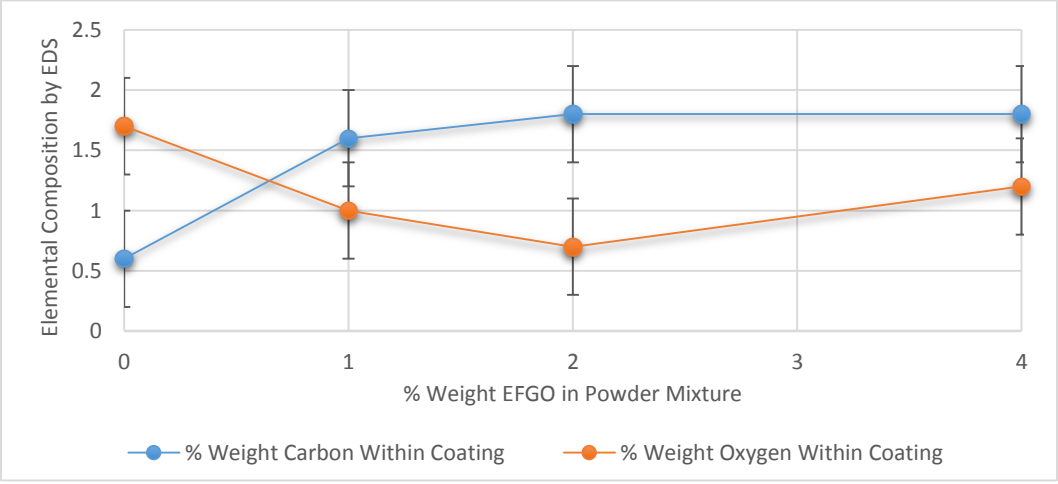

Figure 32: Carbon and Oxygen Content within Coatings via Argon Shroud

The EFGO powder contains Carbon and Oxygen, so the resultant content should increase when deposited in the inert environment. This EDS data, assuming it is valid, may reveal the Argon shroud configuration is not creating an adequate inert atmosphere. Turbulence around the substrate may be disrupting the inert plume, exposing the projectile particles to Oxygen, and combusting the EFGO that is not already inside of a molten Nickel particle. Another explanation is due to a saturation mechanism. Possibly the limited surface area around the Ni-185 particles is enough for 1% weight EFGO to adhere, but any more than that remains loose in the powder. The loose Graphene Oxide has very low density and gets carried away in the flow of gas around the substrate. It was observed that some Graphene Oxide was deposited on the inner wall of the inert shroud.

Claim #7: Solution Suspension Configuration is Inconsistent

The amount of Carbon retained using the Solution Suspension configuration is very good. Too good. The 9.8% weight Carbon content of the coating created using the Solution Suspension using RGO and ethanol is much higher than that of any other coating. This is astounding because the amount of RGO used is very low. The concentration of RGO suspended in the ethanol is 0.1% by weight. The volume flow rate of the ethanol solution was 44 mL/min. This corresponds to a Graphene Oxide mass flow rate of 0.035 g/min. In comparison, the mass flow rate of the Ni-185 powder was 18 g/min. If both were deposited with 100% efficiency, the resulting Carbon content should be very near 0.2%, not 9.8%. The same calculations were carried out for the solution with 0.5% weight EFGO suspended in water, which should have a Carbon content near 0.9%, not 5.2%. These coatings were polished and cleaned multiple times to ensure the Carbon

content is not inflated by polishing artifacts. The only explanation for this is the Graphene Oxide had settled in the bottom of the pressurized tank. A poor suspension could cause the concentration delivered to the substrate early in the process to be much greater than the concentration at the end of the process. This may explain the spherical ~5μm agglomerations of Carbon are inside the coatings, seen in the following figure.

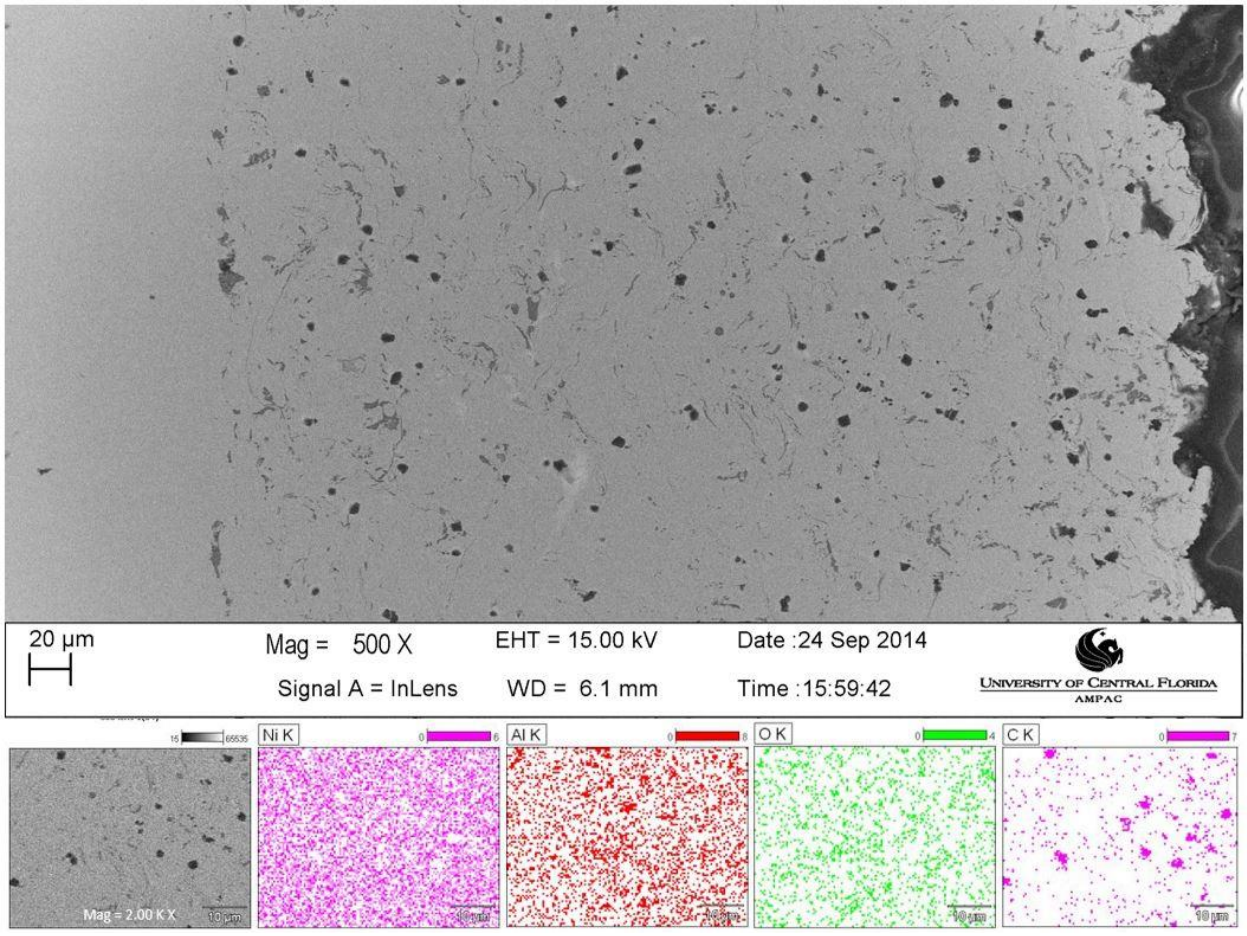

Figure 33: EDS Elemental Map of Ni-Al-RGO Coating via Solution Suspension

This microstructure is unique to the Solution Suspension coatings. Two additional coatings were created to be equal to the coating shown above, but their microstructures were quite different from it and from each other. This method certainly has its issues with

repeatability and real-world practicality. Atomizing water above the plume greatly increases oxide content if done incorrectly. Suspension using ethanol must be done with care since it is literally adding fuel to the fire. With that being said, the coatings containing Graphene Oxide created using the Solution Suspension method were some of the best all-around coatings. Porosity is low, interfaces are good, splat boundaries are thin, thickness is uniform, and microhardness is high.

Claim #8: Argon Shroud Configuration Best Improves Mechanical Properties

The coatings created using the Argon shroud configuration have a better microstructure and fewer irregularities than those created by any other configuration. They also have the lowest standard deviation in microhardness values. The better microstructure makes it more likely the indention does not hit a closed pore or an oxide. The hardest overall coatings were created using the Argon shroud configuration. The configuration is quite repeatable; multiples of a few coatings were sprayed and had nearly identical microstructures, thickness, and microhardness.

The inert shroud has negligible effect on Carbon retention, but it drastically lowers oxide content. SG-100 control coating has 5.7% Oxygen and the SG-100 Argon shroud control coating has 1.7% Oxygen. Furthermore, the carbon distribution is very homogenous compared to that created by the solution suspension configuration. As several have reported with CNT reinforcement, even distribution in the matrix is critical.

Claim #9: CNT Reinforcement is Inconclusive; EFGO and RGO Reinforcement are Similar

Coatings containing Carbon Nanotubes were originally intended to be compared to coatings containing graphene oxide. The CNT required a polymer binder to be mixed with the Ni-5Al powder and were difficult to achieve a homogenous mixture. This led to the creation of a handful of coatings with low hardness and marginal microstructures. These poor results early in the project were eclipsed by the positive results achieved using graphene oxide. Graphene oxide is also more viable for large-scale application due to its relatively low cost. Attention was removed from CNT and, as a result, a fair comparison cannot be made to the graphene oxide coatings. CNT are still included in this thesis for the sake of completeness.

Additionally, coatings containing EFGO and RGO in identical quantities sprayed under identical conditions had very similar properties. The microhardness values for EFGO coatings are greater than the RGO coatings, but they are only slightly beyond error. The microstructures are indistinguishable. The % of irregularities, oxide content, and wear properties are all within error. It appears that the extra production step to reduce the EFGO is not required when improving the mechanical properties of a plasma sprayed metal matrix is the only concern.

Claim #10: Initial Seawater Corrosion Results are Promising

Corrosion tests were performed on select coatings to determine their corrosion resistance to seawater (3.5% NaCl) at room temperature. These Ni-185 coatings can potentially be used as a bond coating under a ceramic (such as Alumina) and used in a seawater environment. In this system, the ceramic provides the corrosion resistance while

the bond coat is used to lessen thermal mismatch between the ceramic and the substrate. However, the ceramic coatings have many pores and may even chip during service, so improving the corrosion resistance of the bond coat by adding graphene oxide would further protect the substrate from corrosion. The following table contains the corrosion results.

Table 9: Seawater Corrosion Resistance of Ni-Al-GO Coatings

Configuration	Additive	Carbon (wt%)	Oxygen (wt%)	Corrosion Potential (mV)	Corrosion Current (μA)
F4 + Soln Susp	0.1% wt RGO	9.8	3	-456	1.08
SG-100	Control	0	5.7	-391	2.26
SG-100	1% wt RGO	1.8	2.1	-450	7.73
Argon Shroud	Control	0.6	1.7	-395	7.87
Argon Shroud	1% wt RGO	4.8	1.4	-355	19.41
Argon Shroud	2% wt EFGO	1.8	0.7	-297	41.47

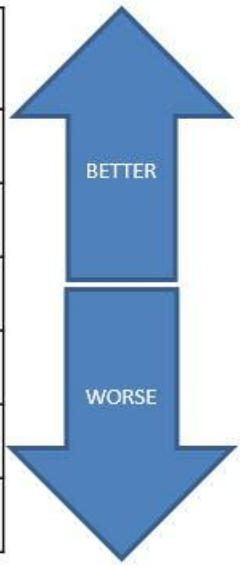

The coating with 2% EFGO has best overall mechanical properties, but it has very poor seawater corrosion resistance. This is because EFGO is hydrophilic. It can be seen that the control samples are better than the coatings containing graphene oxide for the SG-100 configuration and the Argon shroud configuration. This is because the control samples, as detailed in Claim #6, contain more aluminum oxide phases than the coatings containing RGO. The best coating tested for corrosion resistance is the coating produced using the solution suspension configuration with Ethanol and RGO. This coating has a relatively high aluminum oxide content and very high carbon content. This

coating improves the corrosion current twofold over the best control sample that was tested.

Claim #11: TEM Imaging and Analysis Proves Graphene Oxide is Evenly Distributed Within Coatings and Maintains its Structure

Extensive Transmission Electron Microscopy (TEM) analysis was performed on a coating created by the inert shroud method with 2% EFGO. A thin TEM sample was extracted from a mid-coating fracture surface using a Focused Ion Beam (FIB). The following image contains the cross section of the TEM sample prior to extraction.

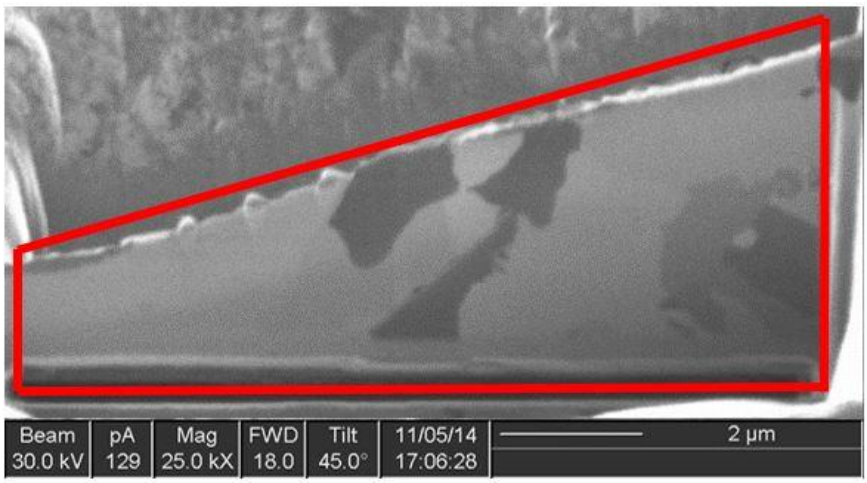

Figure 34: Cross Section of TEM Sample

Several different micron-sized phases can be seen in this cross section. As explained in Claim #7, Energy Dispersive X-ray Spectroscopy (EDS) in a Scanning Electron Microscope (SEM) revealed lighter phases to contain primarily Nickel, the medium phases to contain Aluminum Oxide, and the darkest phases to contain Carbon in select coatings. The following images contain the nano-sized phases observed with the TEM on the light phases believed to be predominantly FCC Nickel.

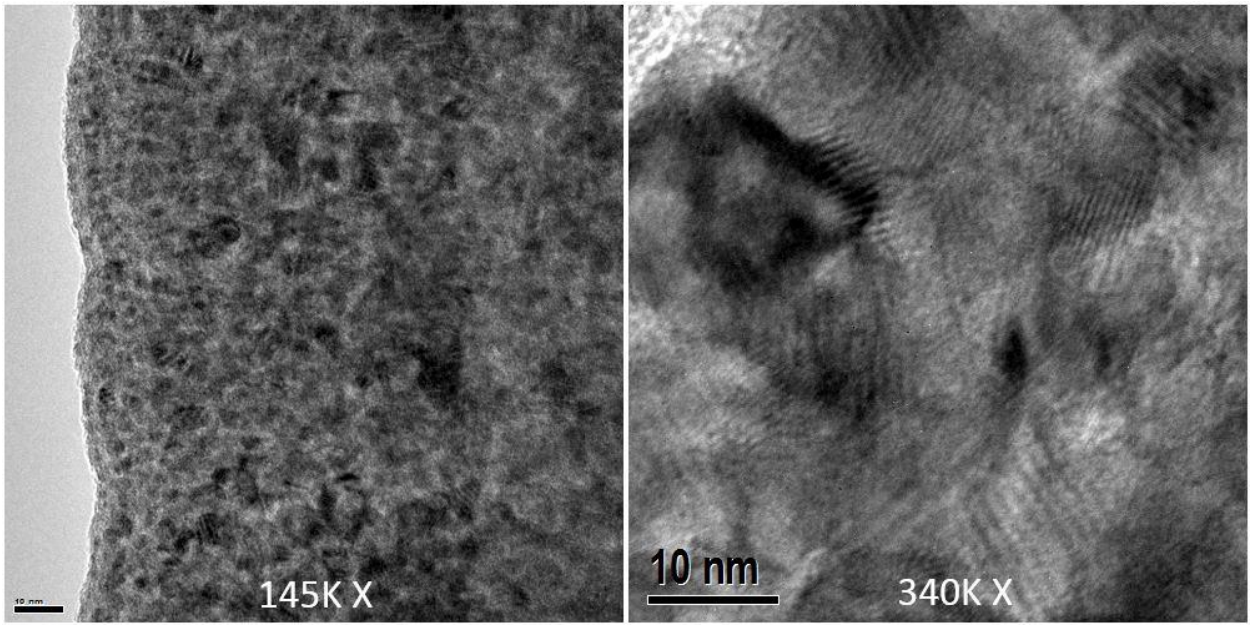

Figure 35: Nanostructure at 145K X (Left) and 340K X (Right)

There are well-defined light and dark regions in the nanostructure and are evenly distributed. The largest of the dark regions are approximately 10nm in diameter, which is approximately the expected size of the EFGO nanosheets. These nanosheets are randomly oriented, so many of them would appear as much smaller than 10nm in a cross-sectional view. The high resolution images contain fringes, indicating crystalline structures, which would also indicate the light regions are an FCC Nickel matrix and the dark regions are graphene oxide. The following diffraction patterns confirm this theory.

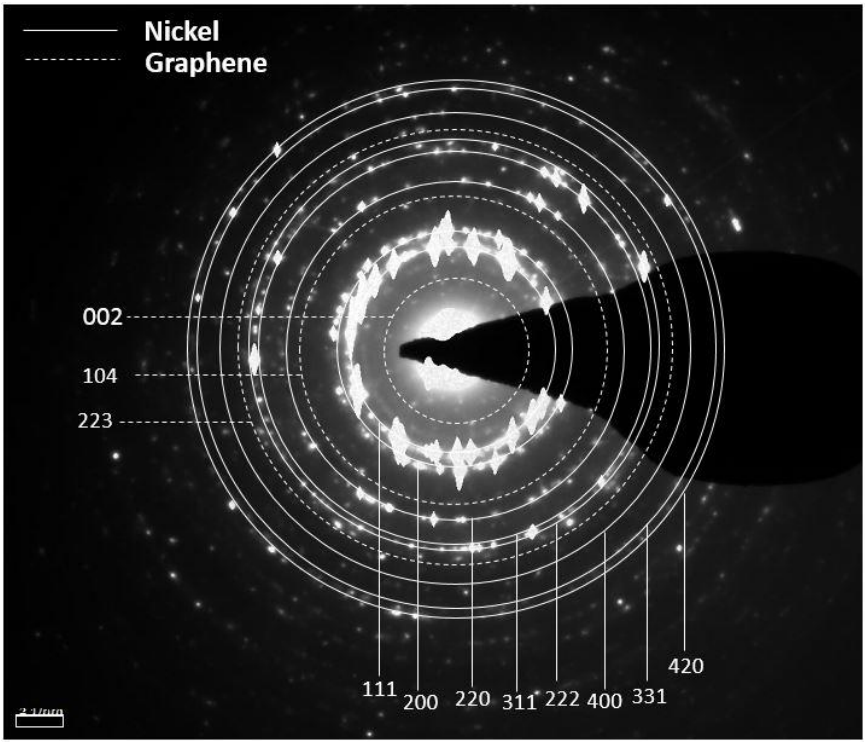

Figure 36: Observed TEM Diffraction Patterns of FCC Nickel and Graphene Oxide

This diffraction pattern is taken over a relatively large area. The rings exist as expected for Nickel and for graphene. Any Aluminum present in this region is in the solid solution of the Nickel matrix and is not greatly affecting the lattice parameter. Next, a diffraction pattern is taken only over a dark region to determine its structure.

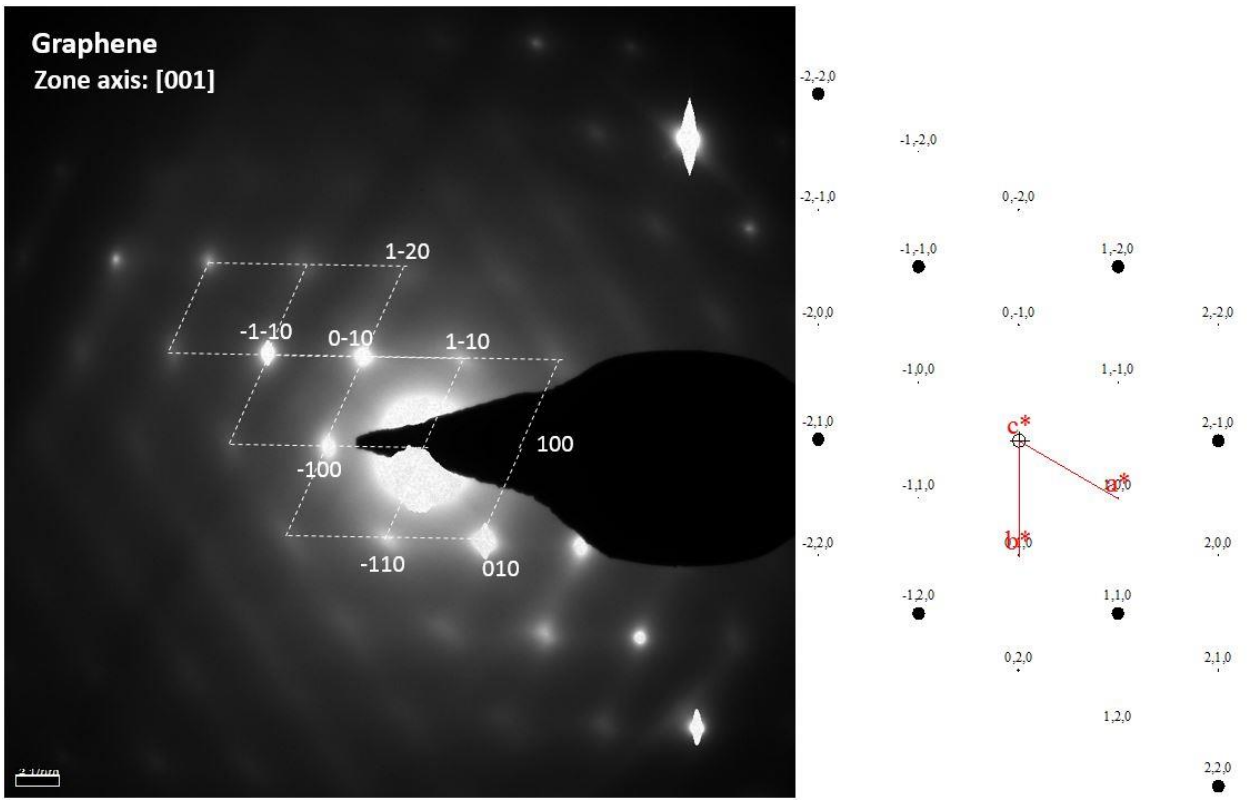

Figure 37: Observed Zone Axis Diffraction Pattern of Graphene Oxide Within Coating (Left) and Theoretical Zone Axis Diffraction Pattern of Graphene (Right)

The hexagonal diffraction pattern observed on a ~10 nm dark region of the coating is exactly the same as the simulated diffraction pattern for graphene. This definitively confirms that the graphene oxide is able to survive the plasma plume and maintain its structure within the metallic coating. These TEM images and diffraction patterns also confirm an even distribution of the graphene oxide sheets. The mechanical strengthening mechanisms of crack bridging, stress transfer, and dislocation strengthening (see Claim #4) are all possible due to this even distribution of graphene oxide that has maintained its incredibly strong structure.

CHAPTER 4: CONCLUSION

Four plasma spray configurations were used in this project to deposit Nickel – 5% Aluminum powder containing small amounts of additive for reinforcement. The four additives used were Edge Functionalize Graphene Oxide, Reduced Graphene Oxide, high quality Graphene, and Carbon Nanotubes. No previous publications have reported the use of Graphene or Graphene Oxide in a thermal sprayed coating. Analysis was performed on 41 different coatings and the results are organized in the following 11 claims:

1. Graphene Oxide increased microhardness (up to 46%)
2. Graphene Oxide increases tensile / adhesion strength (up to 26%)
3. Graphene Oxide reduces the coefficient of friction (up to 18%)
4. There are many possible strengthening mechanisms that can explain the results in claims 1, 2, & 3.
5. Graphene Oxide reduces the coating deposition rate
6. Graphene Oxide has effect on Carbon and Oxygen content within coating
7. The solution suspension configuration is inconsistent
8. The Argon shroud configuration best improves the mechanical properties
9. CNT vs EFGO vs RGO comparison is inconclusive
10. Initial seawater corrosion results are promising
11. TEM imaging and analysis confirms that graphene oxide preserves its structure within the coatings and is evenly distributed

The end result is overall improvement in the mechanical properties of the Ni-5%Al coatings when a small amount of graphene oxide is present. The positive results

achieved in the Ni-5%Al plasma coatings open the door for graphene oxide to be used in many other powder compositions. The Ni-185 used as the model composition in this study is only one of hundreds of commercially available thermal spray powders. The discoveries in this project (configuration development, powder mixing techniques, TEM characterization, etc.) will make it easier for future development of graphene oxide reinforcement in other compositions of metallic thermal spray coatings, possibly leading to widespread use of graphene oxide in the thermal spray industry.

APPENDIX: COMPLETE TABLE OF PLASMA SPRAY PARAMETERS

	Sample 1	Sample 2	Sample 3	Sample 4	Sample 5	Sample 6	Sample 7	Sample 8	Sample 9	Sample 10
Spray Date	5 June	5 June	5 June	26 June	26 June	26 June	26 June	29 June	14 July	27 July
Configuration	F4	F4	F4	F4	F4	F4	F4	F4	F4	Suspension
Current (A)	450	450	450	450	450	450	450	600	600	600
Primary (Ar) Gas Rate (SCFH)	100	100	100	71	71	71	71	85	85	85
Secondary (H) Gas Rate (SCFH)	20	20	20	3.5	3.5	3.5	3.5	20	20	20
Power (kW)	20	20	20	12.5	12.5	12.5	12.5	22	22	22
Standoff Distance (mm)	130	110	90	70	80	60	100	150	150	150
Powder Feed Rate (RPM)	2	2	2	2	2	2	2	2	2	2
Carrier Gas Rate (SCFH)	15	15	15	10	10	10	15	8.5	8.5	8.5
Wt. % Graphene Oxide	0	0	0	0	0	0	0	0	1% EFGO	.01% EFGO
Wt. % CNT	0	0	0	0	0	0	0	0	0	0
Suspension Solution	N/A	N/A	N/A	N/A	N/A	N/A	N/A	N/A	N/A	Water
Suspension Flow Rate (mL/min)	N/A	N/A	N/A	N/A	N/A	N/A	N/A	N/A	N/A	45
Suspension Vertical (mm)	N/A	N/A	N/A	N/A	N/A	N/A	N/A	N/A	N/A	50
Suspension Horizontal (mm)	N/A	N/A	N/A	N/A	N/A	N/A	N/A	N/A	N/A	20
Argon Shroud Pressure (PSI)	N/A	N/A	N/A	N/A	N/A	N/A	N/A	N/A	N/A	N/A
Cycle Sequence	10, 10, 10	5, 10, 10	10, 10	5, 5, 8	5	5, 5	5, 5, 10	5,5	5, 5, 5	5, 5
Total Cycles	30	25	20	18	5	10	20	10	15	10
Robot Speed (mm/s)	300	300	300	300	300	300	300	300	300	300
Coating thickness (microns)	525	600	600	Fail	Fail	Fail	100	500	350	100
Deposition per cycle (microns)	18	24	30	N/A	N/A	N/A	5	50	23	10
Deposition (microns) per second	109	150	188	N/A	N/A	N/A	31	313	146	63

	Sample 11	Sample 12	Sample 13	Sample 14	Sample 15	Sample 16	Sample 17	Sample 18	Sample 19	Sample 20
Spray Date	27 July	30 July	5-Aug	16-Aug	19-Aug	19-Aug	25-Aug	27-Aug	31-Aug	6-Sep
Configuration	Suspension	Suspension	Suspension	F4	F4	F4	Shroud	Shroud	Shroud	Suspension
Current (A)	600	600	600	450	600	450	600	600	600	600
Primary (Ar) Gas Rate (SCFH)	85	85	85	71	85	71	85	85	85	85
Secondary (H) Gas Rate (SCFH)	20	20	20	3.5	20	3.5	5	10	10	20
Power (kW)	22	22	22	12.5	22	12.5	17	18	18	22
Standoff Distance (mm)	150	150	150	80	150	80	110	115	115	150
Powder Feed Rate (RPM)	2	2	2	2	2	2	2	2	2	2
Carrier Gas Rate (SCFH)	8.5	8.5	8.5	10	8.5	10	8.5	8.5	8.5	8.5
Wt. % Graphene Oxide	.5% EFGO	.5% EFGO	.1% RGO	1% EFGO	0	0	1% EFGO	1% EFGO	0	0
Wt. % CNT	0	0	0	0	2.5 w/ APTMS	2.5 w/ APTMS	0	0	2 w/ PEG	0
Suspension Solution	Water	Water	Ethanol	N/A	N/A	N/A	N/A	N/A	N/A	Water
Suspension Flow Rate (mL/min)	45	45	45	N/A	N/A	N/A	N/A	N/A	N/A	45
Suspension Vertical (mm)	50	30	30	N/A	N/A	N/A	N/A	N/A	N/A	30
Suspension Horizontal (mm)	20	65	65	N/A	N/A	N/A	N/A	N/A	N/A	65
Argon Shroud Pressure (PSI)	N/A	N/A	N/A	N/A	N/A	N/A	10 PSI	10 PSI	10 PSI	N/A
Cycle Sequence	5, 5	5,5	5, 5	5,5,5,5	5,5,3	5,5,5,5	1,2 slow	1,1,1	1,1,1	5, 5
Total Cycles	10	10	10	20	13	20	3	3	3	10
Robot Speed (mm/s)	300	300	300	300	300	300	50	50	50	300
Coating thickness (microns)	400	350	450	275	300	125	350	425	275	450
Deposition per cycle (microns)	40	35	45	14	23	6	117	142	92	45
Deposition (microns) per second	250	219	281	86	144	39	122	148	95	281

	Sample 21	Sample 22	Sample 23	Sample 24	Sample 25	Sample 26	Sample 27	Sample 28	Sample 29	Sample 30
Spray Date	6-Sep	12-Sep	12-Sep	12-Sep	12-Sep	12-Sep	12-Sep	19-Sep	24-Sep	24-Sep
Configuration	Suspension	SG-100	Shroud	Shroud	Shroud	Shroud	Shroud	Shroud	Shroud	SG-100
Current (A)	600	600	600	600	600	600	600	600	600	600
Primary (Ar) Gas Rate (SCFH)	85	85	85	85	85	85	85	85	85	85
Secondary (H) Gas Rate (SCFH)	20	10	10	10	10	10	10	10	10	10
Power (kW)	22	18	18	18	18	18	18	18	18	18
Standoff Distance (mm)	150	115	115	115	115	115	115	115	115	115
Powder Feed Rate (RPM)	2	2	2	2	2	2	2	2	2	2
Carrier Gas Rate (SCFH)	8.5	8.5	8.5	8.5	8.5	8.5	8.5	8.5	8.5	8.5
Wt. % Graphene Oxide	0	0	0	.5% EFGO	1% acoustic	4% EFGO	0	1% RGO	2% EFGO	1% EFGO
Wt. % CNT	0	0	0	0	0	0	2.5 w/ APTMS	0	0	0
Suspension Solution	Ethanol	N/A	N/A	N/A	N/A	N/A	N/A	N/A	N/A	N/A
Suspension Flow Rate (mL/min)	45	N/A	N/A	N/A	N/A	N/A	N/A	N/A	N/A	N/A
Suspension Vertical (mm)	30	N/A	N/A	N/A	N/A	N/A	N/A	N/A	N/A	N/A
Suspension Horizontal (mm)	65	N/A	N/A	N/A	N/A	N/A	N/A	N/A	N/A	N/A
Argon Shroud Pressure (PSI)	N/A	N/A	15 PSI	15 PSI	15 PSI	15 PSI	15 PSI	15 PSI	15 PSI	N/A
Cycle Sequence	5,5	5,5	1,1,1	1,1,1	1,1,1	1,1,1	1,1,1	1,1,1	1,1,1	5,5,5
Total Cycles	10	10	3	3	3	3	3	3	3	15
Robot Speed (mm/s)	300	300	50	50	50	50	50	50	50	300
Coating thickness (microns)	450	600	400	300	350	200	325	250	275	600
Deposition per cycle (microns)	45	60	133	100	117	67	108	83	92	40
Deposition (microns) per second	281	375	139	104	122	69	113	87	95	250

	Sample 31	Sample 32	Sample 33	Sample 34	Sample 35	Sample 36	Sample 37	Sample 38	Sample 39	Sample 40
Spray Date	24-Sep	28-Sep	3-Oct	3-Oct	12-Oct	15-Oct	15-Oct	20-Oct	20-Oct	29-Oct
Configuration	SG-100	F4	Shroud	Shroud	Shroud	Shroud	Shroud	Shroud	Shroud	Shroud
Current (A)	600	600	600	600	600	600	600	600	600	600
Primary (Ar) Gas Rate (SCFH)	85	85	85	85	85	85	85	85	85	85
Secondary (H) Gas Rate (SCFH)	10	20	10	10	10	10	10	10	10	10
Power (kW)	18	22	18	18	18	18	18	18	18	18
Standoff Distance (mm)	115	150	115	115	115	115	115	115	115	115
Powder Feed Rate (RPM)	2	2	2	2	2	2	2	2	2	2
Carrier Gas Rate (SCFH)	8.5	8.5	8.5	8.5	8.5	8.5	8.5	8.5	8.5	8.5
Wt. % Graphene Oxide	1% RGO	2% EFGO	1.5% EFGO	3% EFGO	1% EFGO	2% EFGO	0	0	1% RGO	1% RGO
Wt. % CNT	0	0	0	0	0	0	0	0	0	0
Suspension Solution	N/A	N/A	N/A	N/A	N/A	N/A	N/A	N/A	N/A	N/A
Suspension Flow Rate (mL/min)	N/A	N/A	N/A	N/A	N/A	N/A	N/A	N/A	N/A	N/A
Suspension Vertical (mm)	N/A	N/A	N/A	N/A	N/A	N/A	N/A	N/A	N/A	N/A
Suspension Horizontal (mm)	N/A	N/A	N/A	N/A	N/A	N/A	N/A	N/A	N/A	N/A
Argon Shroud Pressure (PSI)	N/A	N/A	15 PSI	15 PSI	15 PSI	15 PSI	15 PSI	15 PSI	15 PSI	15 PSI
Cycle Sequence	5,5	5,5	1,1,1	1,1,1	1,1,1,1,1,1	1,1,1,1,1,1,1	1,1,1,1,1,1	1,1,1	1,1,1,1	1,1,1,1,1
Total Cycles	10	10	3	3	6	7	6	3	4	5
Robot Speed (mm/s)	300	300	50	50	50	50	50	50	50	50
Coating thickness (microns)	450	225	225	200	700	700	700	450	450	600
Deposition per cycle (microns)	45	23	75	67	117	100	117	150	113	120
Deposition (microns) per second	281	141	78	69	122	104	122	156	117	125

REFERENCES

[1] R. C. Tucker, "Thermal Spray Coatings," *ASM Handbook, Volume 5,* pp. 497-509, 1994.

[2] M. Fukumoto and Y. Huang, "Flattening Mechanism in Thermal Sprayed Nickel Particle Impinging on Flat Substrate Surface," *Journal of Thermal Spray Technology,* pp. 427-432, 1999.

[3] K. J. Lee and P. Nash, "The Al-Ni-Ti System," *Journal of Phase Equilibria,* pp. 551-561, 1991.

[4] S. C. Deevi, V. K. Sikka, C. J. Swindeman and R. D. Seals, "Reactive Spraying of Nickel-Aluminide Coatings," *Journal of Thermal Spray Technology,* pp. 335-344, 1997.

[5] S. Deshpande, S. Sampath and H. Zhang, "Mechanisms of oxidation and its role in microstructural evolution of metallic thermal spray coatings - Case study for Ni-Al," *Surface and Coatings Technology,* pp. 5395-5406, 2005.

[6] M. S. Morsi, S. A. Abd El Gwad, M. A. Shoeib and K. F. Ahmed, "Effect of Air Plasma Sprays Parameters on Coating Perfomance in Zirconia-Based Thermal Barrier Coatings," *International Journal of Electrochemical Science,* pp. 2811-2831, 2012.

[7] R. Starosta, "Testing of Regenerative Thermal Spraying Ni-Al Alloy Coatings," *Journal of Polish CIMAC,* 2012.

[8] Sulzer Metco, "Material Product Data Sheet, Nickel - 5% Aluminum," Sulzer Metco, 2014.

[9] ASM Thermal Spray Society, "Accepted Practice to Test Bond Strength of Thermal Spray Coatings," *Journal of Thermal Spray Technology,* pp. 1263-1266, 2013.

[10] R. H. Unger and W. D. Grossklaus, "A Comparison of the Technical Properties of Arc Sprayed Versus Plasma Sprayed Nickel-5 Aluminum," *SAE Technical Paper Series,* 1992.

[11] D. J. Greving, J. R. Shadley and E. F. Rybicki, "Effects of Coating Thickness and Residual Stresses on the Bond Strength of ASTM C633-79 Thermal Spray Coating Test Specimens," *Journal of Thermal Spray Technology,* pp. 371-378, 1994.

[12] V. Pershin, M. Lufitha, S. Chandra and J. Mostaghimi, "Effect of Substrate Temperature on Adhesion Strength of Plasma-Sprayed Nickel Coatings," *Journal*

of Thermal Spray Technology, pp. 370-376, 2002.

[13] O. C. Compton and S. T. Nguyen, "Graphene Oxide, Highly Reduced Graphene Oxide, and Graphene: Versatile Building Blocks for Carbon-Based Materials," *Small Journal,* pp. 711-723, 2010.

[14] Y. Zhu, S. Murali, W. Cai, X. Li, J. W. Suk, J. R. Potts and R. S. Ruoff, "Graphene and Graphene Oxide: Synthesis, Properties, and Applications," *Advanced Materials,* pp. 3906-3924, 2010.

[15] D. A. Dikin, S. Stankovich, E. J. Zimney, R. D. Piner, G. H. B. Dommett, G. Evmenenko, S. T. Nguyen and R. S. Ruoff, "Preparation and Characterization of Graphene Oxide Paper," *Nature,* pp. 457-460, 2007.

[16] J. Wang, Z. Li, G. Fan, H. H. Pang and Z. Chen, "Reinforcements with graphene nanosheets in aluminum matrix composites," *Scripta Materialia,* vol. 66, no. 8, pp. 594-597, 2012.

[17] J. Liu, H. Yan, M. J. Reece and K. Jiang, "Toughening of zirconia/alumina composites by the addition of graphene platelets," *Journal of the European Ceramic Society,* pp. 4185-4193, 2012.

[18] L. S. Walker, V. R. Marotto, M. A. Rafiee, N. Koratkar and E. L. Corral, "Toughening in Graphene Ceramic Composites," *ACS Nano,* pp. 3182-3190, 2011.

[19] M. De Volder, S. Tawfick, R. Baughman and A. J. Hart, "Carbon Nanotubes: Present and Future Commericial Applications," *Science Magazine,* vol. 339, pp. 535-538, 2013.

[20] R. George, K. T. Kashyap, R. Rahul and S. Yamdagni, "Strengthening in carbon nanotube/aluminum (CNT/Al) composites," *Scripta Materialia,* pp. 1159-1163, 2005.

[21] T. Noguchi, A. Magario, S. Fukazawa, S. Shimizu, J. Beppu and M. Seki, "Carbon nanotube aluminum composites with uniform dispersion," *Materials Transactions,* pp. 602-604, 2004.

[22] C. F. Deng, D. Z. Wang, X. X. Zhang and A. B. Li, "Processing and properties of CNT reinforce Al composites," *Materials Science and Engineering: A,* pp. 138-145, 2007.

[23] T. Laha, Y. Chen, D. Lahiri and A. Agarwal, "Tensile properties of carbon nanotube reinforced aluminum nanocomposite fabricated by plasma spray forming," *Composites: Part A,* pp. 589-594, 2009.

[24] K. Balani, S. P. Harimkar, A. Keshri, Y. Chen, N. B. Dahotre and A. Agarwal, "Multiscale wear of plasma-sprayed carbon-nanotube-reinforced aluminum oxide nanocomposite coating," *Acta Materialia,* vol. 56, pp. 5984-5994, 2008.

[25] A. Kukovecz, T. Kanyo, Z. Konya and I. Kiricsi, "Long-time low-impact ball milling of multi-wall carbon nanotubes," *Carbon,* pp. 994-1000, 2005.

[26] A. Esawi and K. Morsi, "Dispersion of carbon nanotubes (CNTs) in aluminum powder," *Composites Part A,* pp. 646-650, 2007.

[27] A. Nieto, A. Kumar, L. Debrupa, C. Zhang, S. Seal and A. Argawal, "Oxidation behavior of graphene nanoplatelet reinforced tantalum carbide composites in high temperature plasma flow," *Carbon,* pp. 398-408, 2014.